PROGRAMA DE DOCTORADO EN INGENIERÍA INDUSTRIAL

TESIS DOCTORAL:

MEJORAS EN INSTRUMENTACIÓN DE ANÁLISIS QUÍMICO DE MUESTRAS EN FASE GASEOSA EN TIEMPO REAL (IMPROVEMENTS ON REAL-TIME, GAS-PHASE, ANALYTICAL CHEMISTRY INSTRUMENTATION)

Presentada por César Barrios Collado
para optar al grado de
Doctor por la Universidad de Valladolid

Dirigida por:
Guillermo Vidal de Miguel

ABSTRACT

In this PhD Thesis, improvements on the elements of a mass spectrometry-based, real-time vapor analyzer were developed. This system is composed of several concatenated stages. Two of them are the focus of this work: the ionizer and the mobility separation. The main objective of this work was to optimize two existing technologies but only as prototypes. The workhorse of this work was numerical simulation. The algorithms were specially formulated and validated.

The ionization technique referred in this PhD Thesis is widely known at academic level as SESI (Secondary Electrospray Ionization). However, it has not been implemented in industry. The results of this work served to design a commercial unit that quintuplicates SEADM's prior SESI-MS sensitivity.

The ion mobility technology referred in this PhD is known as TMIMS (Transversal Modulation Ion Mobility Spectrometry), which at the beginning of this research was a proof-of-concept. The results of this work served to optimize an earlier TMIMS geometry and explain some particularities of the physics involved.

Finally, a practical application is shown (the analysis of volatile organic compounds released by a plant), using the SESI ionizer coupled to a High Resolution Mass Spectrometer. There were two goals in this study. The first was to test the system on a relevant environment, showing the capabilities of SESI-MS on the study of biological systems. Second, this study includes data processing and interpretation (such as relating the detected volatiles with the biological activity), the last step on vapor analysis.

The results shown in this PhD Thesis suggest that a SESI-TMIMS-MS system would be an interesting vapor analysis tool with performance competing with the state-of-the-art dominant technique: GC-MS (Gas Chromatography-Mass Spectrometry).

RESUMEN

En esta Tesis Doctoral se han desarrollado mejoras en los componentes de un sistema de análisis químico de vapores en tiempo real basado en espectrometría de masas. Este sistema está formado por varias etapas conectadas en serie, de las cuáles dos han sido objeto de estudio: la ionización y la separación por movilidad. El objetivo de este trabajo ha sido optimizar tecnologías ya existentes, pero sólo en fase de prototipo. La herramienta de trabajo fundamental ha sido la simulación numérica, que para este trabajo ha tenido que ser formulada y validada.

En el área de ionización se ha trabajado con la técnica SESI (ionización secundaria por electrospray), de sobra conocida en la comunidad académica pero alejada de las aplicaciones industriales. Con los resultados obtenidos en esta Tesis Doctoral se ha llegado a diseñar una unidad comercial que mejora con creces las prestaciones de los sitemas SESI-MS existentes, quintiplicando la sensibilidad.

En movilidad iónica se ha trabajado con la técnica TMIMS (espectrometría de movilidad iónica por modulación transversal), que al comienzo de esta Tesis Doctoral era una tecnología recién dada a conocer a la comunidad académica. Los desarrollos ejecutados en esta Tesis Doctoral han servido para optimizar la geometría y arrojar luz sobre el comportamiento particular del TMIMS.

Finalmente se muestra un estudio real (análisis de los volátiles emitidos por una planta), utilizando el ionizador desarrollado acoplado a un espectrómetro de masas de alta resolución. Este estudio tiene dos funciones. Por una parte, supone una prueba seria , en un entorno relevante (análisis de los vapores emanados por un sistema biológico), más allá de un test de banco de la viabilidad del sistema propuesto. Por otra parte, se cierra el círculo del proceso de análisis de vapores ofreciendo un ejemplo de procesado e interpretación de datos.

Los resultados mostrados en esta Tesis Doctoral auguran que un sistema SESI-TMIMS-MS puede llegar a ser una interesante herramienta de análisis de vapores de prestaciones equiparables (e incluso superiores) a la técnica dominante en el momento de realizar ese trabajo: GC-MS (cromatografía de gases con espectrometría de masas).

CONTENTS

1. Introduction

The development of analytical instrumentation in chemistry, biology or medicine is continuously growing, moving billions of euros worldwide [1], and demanding more sensitive instruments with higher resolution and lower time of analysis. The analysis of vapors, which is the background topic of this PhD Thesis, is related with multiple applications such as security and law enforcement (forensics [2], detection of explosives [3], [4], drugs [5]–[7], illicit substances and chemical warfare agents [8], [9]), environment chemistry [2], [10], medicine (breath analysis and volatiles released from skin [11]–[16]), biology (metabolomics and proteomics [17]–[23]) or chemical and pharmaceutical industries [24].

Traditionally, the analysis of chemical substances in the gas phase has been performed through commercial gas chromatography systems coupled to mass spectrometers (GC-MS), considered the gold standard, and whose inception can be traced back to 1957 [25]. This technique consists on pumping the sample through a capillary column, where different compounds have different retention times. Afterwards, compounds are ionized by electron impact and transmitted into the mass spectrometer. Combining the retention time and the fragmentation pattern, practically any compound can be identified. However, a GC-MS analysis takes too much time to monitor a real-time application, and usually requires sample pre-concentration and derivatization (to chemically modify a compound, so it can be analyzed). Also, temperatures involved and usual ionization methods (typically electron ionization) do fragment the analytes prior to the analysis, so new species whose fragments have not been previously studied cannot be recognized.

An alternative to the GC-MS architecture is to trade the GC process for a secondary electrospray ionizer (SESI) coupled to an ion mobility spectrometer. First, the neutral vapors to be analyzed are exposed to an electrospray plume and ionized [26], [27]. SESI is a soft ionization process which avoids premature fragmentation and needs neither pre-concentration nor derivatization, so the vapors to be analyzed can be directly ingested into the analyzer, in real time. Then, they are separated according to their mobility in the IMS cell [28], [29] in a matter of milliseconds (the GC column separation takes minutes), and finally the mass spectrometer measures both *m/z* and the fragmentation pattern.

The topic of this PhD Thesis focus on improving the SESI ionization and one particular IMS technology, the TMIMS (transversal modulation ion Mobility spectrometry) [30]. In particular, the main objective is to make both technologies more mature. At the beginning of this PhD Thesis, SESI was well-known in academia but not fielded in industry and the TMIMS was a proof-of-concept. Figure 1 shows the SESI-TMIMS-MS architecture. As this system is formed by several modules coupled in series, every stage may be independently studied. The initial motivation of this PhD Thesis focused on implementing numerical simulation tools applied to ion optics in order to optimize the geometries of the SESI ionizer and the TMIMS. At the end, not

only said algorithms were created, but also a pre-commercial SESI source was designed (the results from TMIMS studies were used outside this PhD Thesis). Furthermore, this PhD Thesis includes experimental tests in a relevant environment with the SESI source coupled to a mass spectrometer.
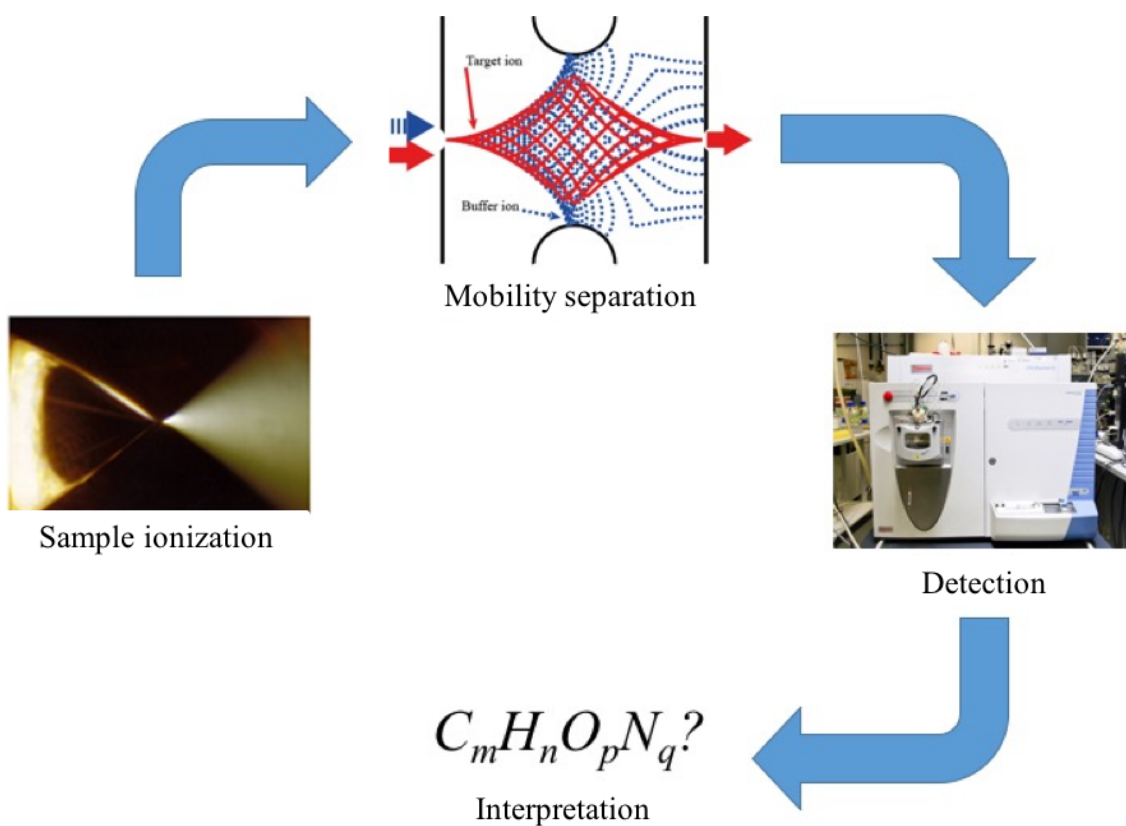
Figure 1 SESI-TMIMS-MS architecture. Image of electrospray for sample ionization extracted from [31]. Mass spectrometer for detection image corresponds with a Thermo-Fisher Orbitrap instrument

2. State of the art

2.1. Vapor ionization

2.1.1. SESI ionization

Secondary electrospray ionization (SESI) was first proposed by Nobel Prize winner John B. Fenn [32] as an application to volatile analysis of his work on electrospray Ionization (ESI) of proteins and other non-volatile solutes. ESIs, coupled to Liquid Chromatography instruments and Mass Spectrometers (LC-MS) are commonly used to study non-volatile substances. Although volatile analysis through SESI is not widely used, it has shown great potential since H. H. Hill works [5]. By means of SESI ionizers substances of very low volatility can be ionized, without derivatization, and it is possible to perform real-time analysis. SESI is being successfully used in, among other applications, explosive, drug and illicit substances detection [3], [5], [6], [33], human breath and skin metabolite analysis [11], [13], [34], [35], food analysis [36], [37] and bacterial identification [38]–[40]. SESI-MS can detect compounds with very low volatility (e.g. urea in breath has vapor pressure in the order of 10^{-5} *torr*), in very low concentrations (trace detection of explosives in the range of *ppqv* [41]) and extending the molecular weight range far beyond *300 Da* (which is the limit in current commercial alternatives).

A SESI ionizer works in the following way. First, an electrospray is formed when a strong electric field is applied on a conducting liquid (typically an acidic or basic solution) droplet formed in the tip of a micrometric capillary. Charges are regrouped on the surface where Coulomb forces break surface tension. The droplet then adopts a conical shape called Taylor cone (instead of the classical sphere) and emits highly charged droplets whose diameter is in the range of nanometers. These droplets evaporate fast resulting in suspended ions which mix with the neutral vapors to be analyzed and transfer the charge to them. Ionized vapors have to be extracted from the ionization chamber efficiently to avoid saturation caused by Coulomb repulsion. Equation (1) shows the maximum ion concentration (N_S),

$$N_S = N_V \frac{k\varepsilon_0}{eZ_S} \approx 10^{-4} N_V \qquad\qquad (1)$$

where N_V, Z_S, e, k y ε_0 are the concentration of neutral vapors, the ionic mobility, the ion net charge, the collision rate between the neutral vapors and the electrospray charging agents and the vacuum permittivity respectively. Figure 2 shows a photograph of the electrospray tip and the ionizing ion cloud.
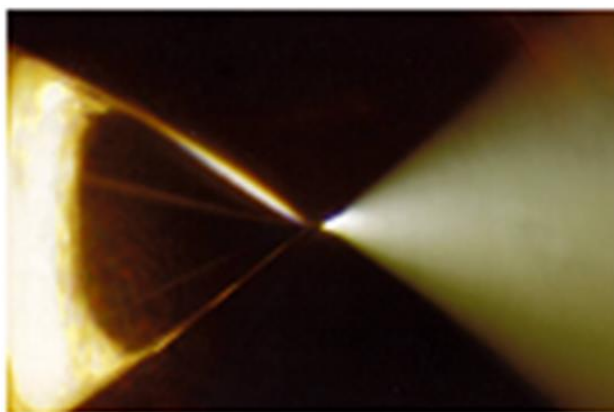
Figure 2 Electrospray [31]

There are two main drawbacks that have avoided SESI generalization. On the one hand, there are not SESI ionizers which can be easily coupled to commercial mass spectrometers. On the other hand, SESI ionizing mechanism is still not well understood, which makes harder to optimize design and operation parameters.

2.1.2. Low Flow SESI (LFSESI)

SESI ionizers require high sample flows (*~5 L/min*) in order to raise ionization efficiency. However, the analytes of interest are too diluted. This effect is even worse taking into account the mass spectrometer counter flow which avoids contamination and cluster formation. So, the sensitivity is limited. Downsizing dramatically the sample flow (by 100-fold) raises the sensitivity up to one molecule in a quadrillion [41]. This Low Flow SESI (LFSESI) configuration is shown in Figure 3, which separates the ionization region from the clean gas region by adding a new electrode (impaction electrode).
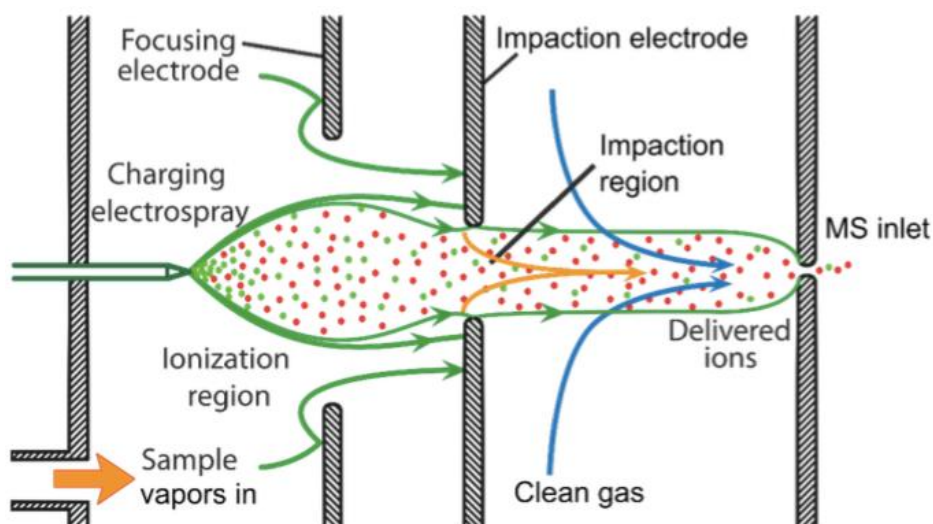
Figure 3 LFSESI schematics [42]

2.2. Ion mobility
2.2.1. Theory

When an ion moves inside a gas due the presence of an electric field, ion mobility, Z, is defined as the proportional constant between the electric field, E, and the ion terminal velocity, v, (2),

$$\vec{v} = Z\vec{E} \tag{2}$$

The ion accelerates due the electric field, but collides against the gas molecules, losing kinetic energy. The force that pushes forward the ion is a function of the electric charge, and the drag force depends on the geometry of the ion and the nature and thermodynamic state of the gas. So, ion mobility is a property of both the ion and the environment, and strictly also a property of the electric field. However, for weak electric fields ($E/N<2\cdot10^{-17}$ $V\cdot cm^2$, where N is the gas molecular density), mobility is approximately constant with electric field and can be estimated through Mason's equation (3),

$$Z = \frac{3e}{16N}\sqrt{\frac{2\pi}{\mu k_B T}}\frac{1}{\Omega} \tag{3}$$

where e, μ, k_B, T and Ω are the ion charge, the ion-gas pair reduced mass, the Boltzmann constant, the thermodynamic temperature and the collision cross-section respectively. Empirically, Mason's equation approximates the order of magnitude of the mobility value, as some factors can only be determined experimentally. In particular, for strong electric fields, mobility can be calculated as follows (4), where Z_0 is given by Mason's formula and a, b, etc. are determined experimentally.

$$Z(E) = Z_0\left[1 + a\left(\frac{E}{N}\right)^2 + b\left(\frac{E}{N}\right)^4 + \cdots\right] \tag{4}$$

Early IMS instruments were developed in the 1960s, and have been used since then in military or enforcement applications such as explosives, narcotics and illicit substances detection [5], [33]. Combined with MS, interest in IMS-MS techniques has been increased in chemical and pharmaceutical industries, and in medicine as a tool for proteomics and metabolomics [18], [21]. IMS-MS tandem not only informs about the mass of molecules, but also about geometries which, among other things, can be used to identify isomers or different molecule bindings.

2.2.2. Instrumentation

Drift Tube IMS (DTIMS) [43]–[49] was the first IMS development, and is the most popular IMS due its simplicity, robustness, quickness, compact size and low energy requirements. It consists on a tube where ion packets travel at different velocities according their mobilites and are classified in function of their flight time. Then, separation depends on tube length and applied voltages. Its main disadvantage is that it transmits a pulsed signal which is complicated to synchronize with other instruments.

Field Asymmetric Waveform IMS (FAIMS), also known as Differential Mobility Spectrometry (DMS), [50]–[57] applies spatial separation to ions and produces a continuous output. It takes advantage of mobility differences between strong and weak electric fields. Only ions whose displacements due to a pulsating strong field are compensated by a stationary weak one are outputted from the mobility cell. Its main drawback is that it does not separate by means of true mobility.

Travelling Wave IMS (TWIMS) [58]–[61] [58]–[60] devices are similar to DT-IMS. It also produces a pulsed output, but in this case ions are dragged by a voltage wave train. Its main disadvantage is that implies low operation pressure (these devices are integrated inside the mass spectrometer) and the high energies involved may fragment ions.

Differential Mobility Analyzer (DMA) [62]–[66] uses two orthogonal fluid and electric fields, so the composition of velocities results in different trajectories and one of then reaches the exit. It provides a continuous output, high transmission and operates at atmospheric pressure. However, issues related to turbulence and compressible flow (due high gas velocity is necessary) make DMA design bulky and manufacturing requires very high quality tolerances and surface finishing.

Trapped IMS (TIMS) [67], [68], confines selected ions by means of opposing non-uniform electric field and a gas flow. Then, these ions are released to the detector.

Open Loop IMS (OLIMS) [69], [70], also known as Aspiration IMS (AIMS), consists on a gas flow pushing ions into an array of pairs of electrodes, orthogonal to the flow direction, which attract ions. Electrodes work as detectors.

Overtone Mobility Spectrometry (OMS) [71]–[75] concatenates several identical drift regions, each with an elimination region and a transmission region. Electric fields are modulated to allow only a narrow range of mobilities to exit the device. A continuous ion flow is outputted.

2.2.3. TMIMS

Transversal Modulation IMS (TMIMS) [30], [76]–[80] uses only electric fields to provide a continuous output, operating at atmospheric pressure. Ions are driven by an axial steady and a transversal, oscillating electric fields. Ions get inside through a narrow slit, and only those whose trajectories are complete oscillations at a given

frequency can reach the outlet slit. Every mobility is associated to a frequency (resonant frequency). Figure 4 shows a schematic of the basic TMIMS configuration (a single filtering chamber with two planar electrodes and two cylindrical electrodes for the steady and the oscillating field respectively) with three characteristic ion behaviors: a) selected ions; b) faster ions, which do not complete even a single oscillation; and c) slower ions, which complete more than a single oscillation. TMIMS oscillating electric field can be disabled so all ions are allowed to exit the mobility cell.
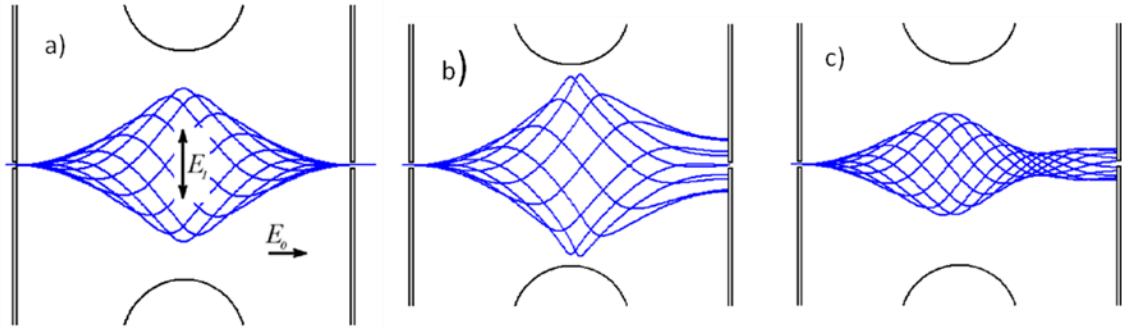
Figure 4 TMIMS working principle: a) selected ions; b) higher mobility ions; c) lower mobility ions [81]

Early theoretical approximations to TMIMS considered uniform electric fields [30]. The landing point on the second axial electrode, *Y*, considering a sinusoidal oscillation and convective trajectories with infinitesimal thickness is defined in (5), where *Y=0* represents the outlet slit,

$$Y = 2\frac{ZE_1}{\Omega}\sin\left(\frac{\Omega l}{2ZE_0}\right)\sin\left(\Omega t - \frac{\Omega l}{2ZE_0}\right) \tag{5}$$

where *E₁, l, t, Ω* y *E₀* are the transversal field amplitude, the TMIMS length, time, the transversal field angular frequency and the axial electric field respectively. For selected ions, *Z=Ωl/(2E₀π)*, the first sinus is equal to zero, so they always reach the outlet. However, for the rest of the ions the second sinus is periodically equal to zero, so there is an undesired ion pulse. This problem can be resolved by adding a second stage *π/4* out-of-phase (Figure 5, [77]), or several in-phase stages (*TMIMS Ladder*, [82]).
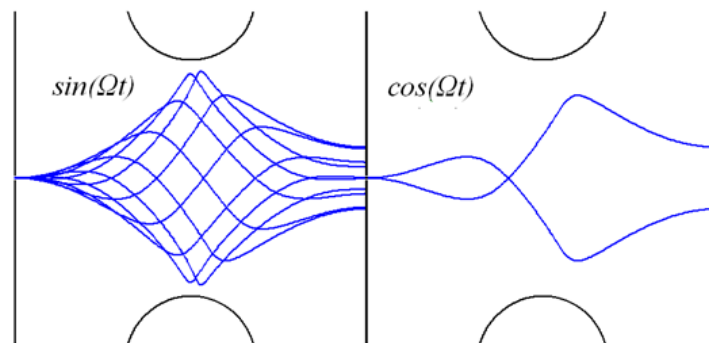
Figure 5 Elimination of the undesired pulsed signal in TMIMS [81]

On the other hand, the first sinus is also canceled when its inside is equal to a multiple of π. That means not only ions with $Z=\Omega l/(2E_0\pi)$ reach the outlet, but also ions with mobilities $Z/2$, $Z/3$, etc. (Figure 6). In order to eliminate these multiple resonances, a pre-filtering stage should be added upstream the TMIMS (*Travelling Gate*, [83]).
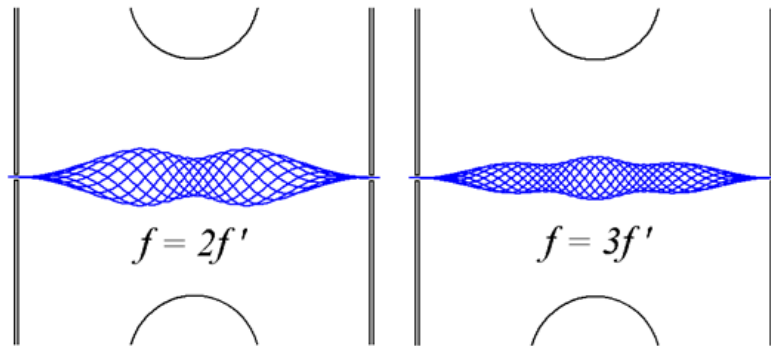
Figure 6 Overtones in TMIMS [81]

3. Purpose of this PhD Thesis

3.1. General objectives

SESI and TMIMS are two technologies that only exist as prototypes at some research facilities, and they are not commercially available because they have not achieved enough technology readiness level.

SESI ionizers could be used in multiple applications such as metabolite identification from biofluids or explosive trace detection. However, none of the major MS manufacturers have integrated SESI in their portfolios. There are two main reasons: interfacing SESI with the MS is rather difficult and the knowledge of SESI mechanism is not enough to optimize design variables.

In the case of TMIMS, this is a relatively young technology (patent application sent in 2009 and approved in 2013 [76]). At the beginning of this PhD Thesis it had recently been presented to academia as a proof of concept, and only two prototypes and a simple theoretical model based on uniform fields (without geometry considerations) existed. Despite being qualitatively accurate, this theoretical model did not match experiments quantitatively.

Then the main objective of this PhD Thesis is to increase the maturity level of these technologies. In the case of SESI ionization, the final goal is to obtain a commercial SESI system, tested in a relevant environment. For TMIMS, the objective is to develop simulation tools to evaluate performance and optimize the design.

3.2. Particular objectives in SESI research

The particular objectives for the SESI research are the following:

- **Development of simulation tools.** Earlier SESI designs were based on qualitative estimations. The main novelty of this research is the inclusion of numerical simulation which comprises fluid dynamics, electrostatics, transport of diluted species and reactive flow. Specifically, the key highlight is the numerical model of the electrospray, which is affected by singularities and there is not much literature about it.
- **Mechanical/Electrical design of the SESI ionizer.** The mechanical design is much more ambitious than a proof-of-concept demonstrator. The SESI source developed is a fully commercial unit, which has to be robust, easy to use, and requiring low maintenance. Also, it hast to be compliant with the required normative.
- **Characterization of the SESI ionizer and benchmarking against the state of the art.**
- **Testing the SESI ionizer in a relevant environment.**

3.3. Particular objectives in TMIMS research

The particular objectives for the SESI development are the following:

- **Development of a simulation tool to optimize geometry.** Due to the lack of a reliable theoretical model which matches quantitatively experimental data, a computational model was required. This simulation tool is built from scratch to be validated experimentally and perform parametric studies.
- **Development of a simulation tool which includes space charge.** The former simulation tool was only valid when reproducing determined experimental conditions. This second iteration of the simulation tool includes space charge and offers a closer approximation to TMIMS real experiments.

3.4. Structure of the PhD Thesis

This PhD Thesis is composed of four parts: (i) SESI ionization; (ii) TMIMS: geometry optimization; (iii) TMIMS: space charge; and (iv) testing in a relevant environment. This structure follows the natural process of the proposed vapor analyzer. First, samples are ionized. Then, the mobility cell selects the compounds of interest. And finally, the results are interpreted according to the particular application.

4. Methods

4.1. Numerical simulation

One of the key methods in this PhD Thesis is numerical simulation. The instruments developed were mere prototypes at the beginning of this PhD Thesis. Computational methods have supplied large amounts of quantitative information in a relatively easy and fast way. However, all this research was not only executing parametric sweeps with said methods. Computational tools had to be created and validated for both SESI and TMIMS.

In the case of the SESI ionizer, a numerical method which combines fluid mechanics, electrostatics, transport of diluted species and reactive flow was implemented. The highlight of this algorithm is the electrospray model, which is affected by singularities and there is not much literature about this topic.

In the case of the TMIMS, the simulation algorithms were defined from the beginning. Simplification hypothesis required an exhaustive study of the involved physics. An important obstacle was to make compatible the scales of the different phenomena.

4.2. Mechanical/electrical design

Mechanical/electrical design was other kind of methodology used in this PhD Thesis. The conclusions extracted from numerical simulation were brought to a real design, which implied to deal with restrictions imposed by the real world such as viability of manufacturing, selection of commercial parts or safety standards. This methodology was applied in the SESI development. Data from simulations was used to optimize the internal geometry of the ionization chamber. However, the SESI ionizer comprises a series of supporting layers to provide voltages, temperature control, isolation, interfacing to mass spectrometer, mechanical alignment or electrospray liquid. The final result is a plug&play instrument which can be coupled to a commercial mass spectrometer in a matter of minutes.

4.3. Experimental studies

Applied exclusively to the SESI line of research, experimental studies were the final step to complete its development. Once the device was manufactured and assembled, its performance was characterized and benchmarked against a state-of-the art SESI source. Finally, the developed SESI ionizer was tested in a relevant environment.

4.4. Resources

This PhD Thesis would have not been possible without the support of the R&D SME Sociedad Europea de Análisis Diferencial de Movilidad (SEADM S.L.) and the Research Group of Professor Renato Zenobi at the Laboratory of Organic Chemistry of

5. Part I. SESI ionization

The first part of this PhD Thesis is dedicated to the SESI ionizer. The first half of this research describes the implementation of a numerical method which combines fluid mechanics, electrostatics, transport of diluted species and reactive flow to simulate the SESI process. The main highlight of this part is the electrospray modeling into a Finite Element Method algorithm. The second half shows some experimental results with the optimized SESI source derived from the simulations like benchmarking against a state-of-the-art ionizer. The results were published in the follow scientific paper:

- Barrios-Collado, C.; Vidal-de-Miguel, G.; Martínez-Lozano Sinues, P. Numerical Modeling and Experimental Validation of a Universal SESI Source for Mass Spectrometric Gas Analysis in Real-Time. *Sensor Actuat B-Chem* **2016**, 223, 217-225

5.1. Methods

The mathematical model described by Fernandez de la Mora [84] is based exclusively on electrostatics for the emission of electrified liquid cones and has the following assumptions: (1) the meniscus and the spray form two ideal and infinitely large opposed cones; (2) it ignores the microjet that transitions between the meniscus and the expanding plume, and the droplet formation dynamics; (3) the liquid is infinitely conducting (adequate for conductivities higher than *0.03 S/m*); (4) all droplets have the same charge, size and electrical mobility; (5) it neglects droplets inertia, evaporation, diffusion and the scale of the micro-jet. Although this model is limited to the ideal case of an electrospray plume expanding to infinity, it is valid in the proximity of the meniscus tip because its length-scale is far smaller than the meniscus itself. The singularity region and the far field region can be easily modeled, but the physical processes taking place in the transition region are far more complex. Since spherical symmetry is conserved along the transition region, and given that diffusion effects are negligible in this region (due to the high ionic velocities), it can be assumed that the charge concentration defined in [84] can be directly inputted in the spherical interface between the transition region and the far-field region.

Figure 7 shows a scheme of the domain shape that incorporates a spherical cap centered about the electrospray tip, as well as a conical meniscus. The radius r_0 of the cap was half the capillary radius, and the electric potential and the ion concentration boundary conditions on the cap were defined in accordance with the analytical solution for free space or spray at radial coordinate r_0, given by [84]. The meniscus and spray angles α and β were interpolated from tabulated data, as a function of: (i) $G(\alpha) = I/(2\gamma Z)$; ii) the spray current (I); (iii) the liquid surface tension (γ) and (iv) the ion mobility (Z). The electric potential (V) and the charge concentration (ne^-) followed (6) and (7), respectively:

$$V = \begin{cases} V_0 - \sqrt{\dfrac{2I\sin 2\alpha\, r}{3\pi\varepsilon_0(1+\cos\beta)Z}\,\dfrac{P(\alpha)Q(\theta)-Q(\alpha)P(\theta)}{0.63662}}, & \alpha \leq \theta \leq \beta \\[2em] V_0 - \sqrt{\dfrac{4Ir}{3\pi\varepsilon_0(1+\cos\beta)Z}}, & \beta \leq \theta \leq \pi \end{cases} \qquad (6)$$

$$ne^- = \begin{cases} 0, & \alpha \leq \theta \leq \beta \\[1.5em] \sqrt{\dfrac{3\varepsilon_0 I}{4\pi(1+\cos\beta)Zr^3}}, & \beta \leq \theta \leq \pi \end{cases} \qquad (7)$$

where V_0, θ, $P(\theta)$ and $Q(\theta)$ are the electrospray voltage, the angular coordinate and two independent Legendre functions of degree $1/2$ and order 0.
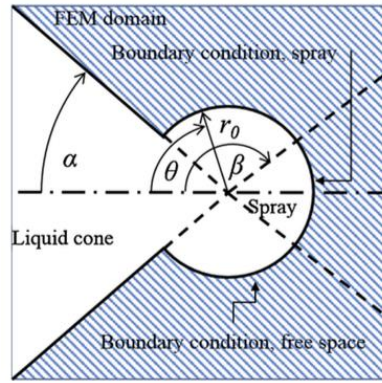
Figure 7 Numerical model of the electrospray

According to the Fuchs and Sutugin evaporation model [85], the droplet mass loss follows $d_{d0}{}^2 - d_d{}^2 = 4/\rho_d D_{vs} c_s(1+K_n)/(1+1.71K_n+1.33K_n{}^2)t$, where D_{vs}, and c_S and K_n are vaporized solvent diffusivity, the concentration of vaporized solvent on the droplet surface and the Knudsen number, respectively and d_{d0} is the initial droplet diameter. Assuming $K_n = 1$ (transition regimen), $D_{vs} = 2 \cdot 10^{-5}$ m^2/s (based on water vapor diffusivity on air), $c_S = 0.024$ kg/m^3, $d_{d0} = 0.2$ μm and that after evaporation $d_d \ll d_{d0}$, the characteristic time of evaporation is around $40\ \mu s$, which implies a displacement of $100\ \mu m$. This estimation is conservative, as it does not take into account the loss of solvent mass due Coulomb explosions. As the length of the ionization region is in the order of $10\ mm$, the conclusion is that SESI ionization reactions took place where droplets are already evaporated [86].

The evolution of the concentrations was modeled according to the differential equations system given by (8) which includes the reaction kinetics as well as the convective and diffusive transport,

$$\begin{cases} \left(Z_c\vec{E} + \vec{v}_f\right) \cdot \nabla c_c + \dfrac{Z_c c_c^2 e^-}{\varepsilon_0} = -kc_c c_v + \dfrac{Z_c k_B T}{e^-}\nabla^2 c_c \\[2mm] \vec{v}_f \cdot \nabla c_v = -kc_c c_v + D\nabla^2 c_v \\[2mm] \left(Z_i\vec{E} + \vec{v}_f\right) \cdot \nabla c_i + \dfrac{Z_i c_c c_i e^-}{\varepsilon_0} = kc_c c_v + \dfrac{Z_i k_B T}{e^-}\nabla^2 c_i \end{cases} \qquad (8)$$

where c_c, Z_c, c_v, c_i and Z_i are the concentrations and mobilities of charging ions, neutral vapors and ionized vapors respectively; E, v_f, k_B, T and D are the electric field, the fluid velocity, the Boltzmann's constant, the absolute temperature and the neutral vapor diffusivity respectively; and k is the reaction kinetic constant. SESI process is thought to occur by, first ejection of hydronium clusters from the electrospray, which lead to gas-phase proton transfer reaction to neutral vapors [86]. Typical values for ion-molecule reaction rate constants for proton transfer reactions range between 10^{-9} and $5 \cdot 10^{-9}$ cm^3/s [87]. For such product ions, typical electrical mobilities lie in the range $Z_i \sim$ 1–2 $cm^2/V/s$. These k and Z_i values can finally be used to bracket the dimensionless probability of ionization $p_i = c_i/c_v = k\varepsilon_0/e^-/Z_i$ [26], where ε_0 is the vacuum permittivity and e^- the ionized vapor charge. Typical p_i values range between 10^{-3} and 10^{-4}.

The boundary conditions for neutral and ionized vapors at the spherical cap have to be calculated. Due the high concentration of charging ions in this region, a significant loss of neutral vapors is expected. Recent analysis by Juan Fernández de la Mora for a conical electrospray that expands and mixes with a neutral vapor shows that, in absence of diffusion, (8) can be integrated for neutral vapors. The concentration of neutral vapors is given by $c_v/c_{v0} = \exp(-kc_c r/v_f)$, where r and c_{v0} are the radial coordinate and the concentration of neutral vapors at the ionizer inlet. Similarly, for ionized vapors at the same conditions, the concentration is given by $c_i/c_{v0} = p_i\exp(-kc_c r/v_f)$.

The typical Reynolds number is $Re \sim 709$, which is well below the critical Re (~ 2000). Accordingly, a laminar flow model was used. The domain included a sample inlet, an outflow to the MS capillary inlet. The numerical model was implemented in commercial FEM software COMSOL Multiphysics. The model was built considering axial symmetry and iterative mesh refinement. The algorithm re-meshed those areas affected by high gradients, such as the areas close to the electrospray tip, the MS inlet, and the boundary layers that separate the plumes from the clean regions.

An optimized ionizer was built accordingly with the numerical results, and benchmarked its performance against a classical ("standard") SESI source (a nano-spray emitter enclosed in a cylindrical chamber facing the MS orifice). To validate the SESI sources, precise amounts of target vapor species were delivered and measured the resulting mass spectral signal intensity [3], [8], [14]. The species of interest were diethylamine (DEA) and the drugs melatonin, propofol, paracetamol, pentobarbital and midazolam.

5.2. Results

The numerical model for the electrospray was validated by simulating the experiment described in [84], which is shown in Figure 8 (*this figure replaces the one in the original publication as it is more accurate, and the experimental and simulated meniscus angles can be compared*). In this experiment, a capillary of *1 mm* external diameter and *0.806 mm* internal diameter sprays a solution of H_2SO_4 (5%) in 1-octanol ($\gamma = 35$ *dyn/cm*; $Z = 0.307$ *cm²/V/s*) at *3715 V* against a grounded plate at *7 mm* from the tip. The radius r_0 where the analytical solution is implemented is 1/100 the capillary internal diameter.
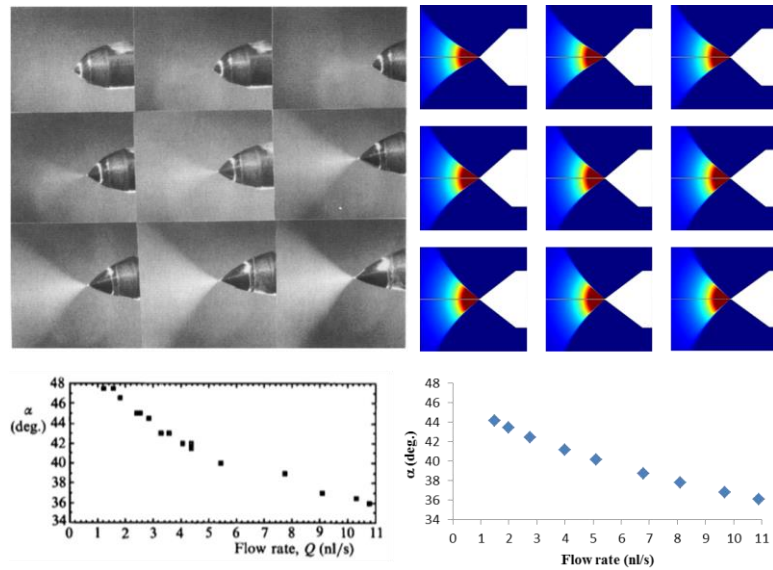
Figure 8 Experimental (left, reproduced with permission form [84]**) and simulated (right) electrosprays. From left to right and top to bottom, the electrospray flow rate in nL/s are: 1.5; 2.0; 2.75; 4.0; 5.1; 6.8; 8.1; 9.7 and 10.9.**

Figure 9a–c show the surface plots of the concentrations of charging ions (c_c), neutral vapors (c_v), and ionized vapor (c_i). Figure 9d–f show the corresponding concentration profiles of charging ions, neutral vapors and ionized vapors along the radial coordinate. The simulations considered a realistic scenario where the charging ions (H_3O^+) were produced from an electrospray of water (*0.1%* formic acid) and *8.5 ppt* of DEA as neutral vapors. As expected, close to the electrospray tip the concentration of charging ions is very high, and it decreases quickly with the distance to the electrospray tip (noticeable in the logarithmic scale). The ionization region has the same shape as the electrospray plume, but the concentration of ionized vapors is far lower than the charging ions concentration. This supports the hypothesis of theoretical models that electric field distortions due to space charge are essentially caused only by the charging agent. There is a significant decrease of neutral vapor concentration along the electrospray plume (Figure 9b and e). Due to the low p_i ($\sim 10^{-3}$–10^{-4}), it is commonly accepted that the concentration of neutral vapors should be constant [26], [27]. However, the simulations suggest that electric fields drive ionized vapors outside the ionization region too fast to be replaced by fresh neutral molecules. This effect

causes a loss of neutral molecules in the core of the electrospray plume and makes the highest concentration of ionized vapors on the periphery of the plume, where fresh neutral molecules and charging ions meet easier. Upon lowering the sample flow, this phenomenon gets more visible. Diffusion plays a key role in neutral vapors transport at low flows ($\sim 10^{-2}$ *L/min*), where Péclet numbers are in the order of *1*. Hence the importance of including diffusion in this model. However, for charging ions and ionized vapors, as expected from the high Péclet numbers ($\sim 2 \cdot 10^{5}$), diffusion effects are noticeable only at the borders of both clouds.
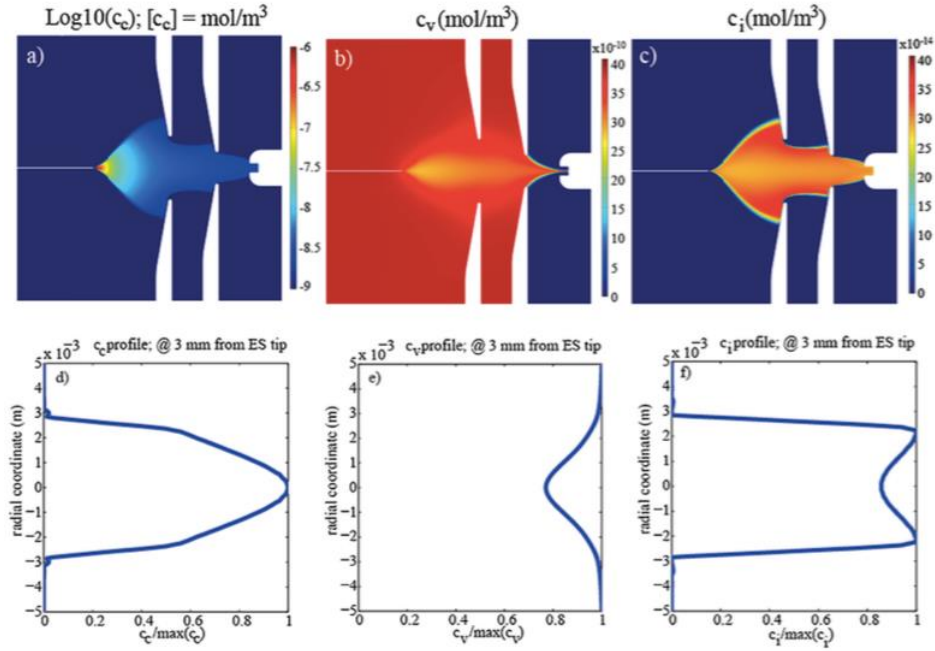
Figure 9 Contour plots and radial profiles of the concentration of the involved species: (a, d) charging ions; (b, e) neutral vapors; (c, f) ionized vapors

The theoretical ionization efficiency is given by $\eta_i = p_i q_{ms}/q_s$, where η_i, q_{ms} and q_s are the ideal ionization efficiency, the flow entering by the MS (*1.6 L/min*) and the sample flow, respectively. The simulated ionization efficiency was calculated as $\eta = c_i q_{ms}/(c_{v0}q_s)$. Figure 10a shows a comparison of ideal and simulated ionization efficiencies for four different electrospray currents (20, 50, 100 and 200 nA) as a function of sampling flow rate. At high sample flows, η follows η_i. η increases as the sample flow is reduced because the neutral vapors are concentrated. At flows below *0.2 L/min*, although it still increases, it is clearly lower than η_i due the loss of neutral vapor concentration along the electrospray plume. This effect becomes more dramatic with increasing electrospray currents, as c_c becomes higher. At such conditions, the real probability of ionization is lower than p_i and becomes dependent on q_S and I. As an extended exercise of this observation, Figure 10b shows a dimensionless representation of the ratio η/η_i. vs. q_s/q_{ms}. The figure shows the results for the combination of three different paired kI values, which are proportional to the term kc_cc_v in (8). There are three clusters for each kI group and a closer ideal behavior for smallest kI product.
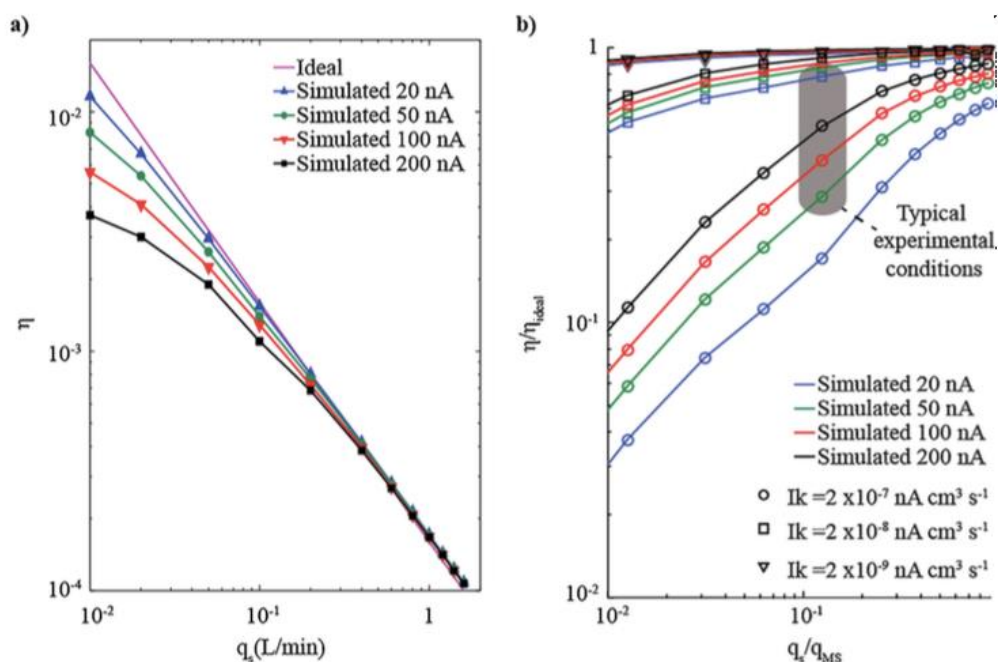
Figure 10 a) Ideal and simulated ionization efficiency; b) ratio between simulated and ideal efficiencies vs. sample flow rate over MS flow rate (the area covering typical experimental conditions is shaded).

Figure 11a compares the performance of the optimized LFSESI ionizer built according to the simulation results against a classical SESI. The efficiency of the optimized LFSESI is five times greater than the standard SESI. Figure 11b shows the detection of several drugs of interest ionized with the optimized LFSESI, achieving limits of detection of tenths of *ppt* in gas phase.
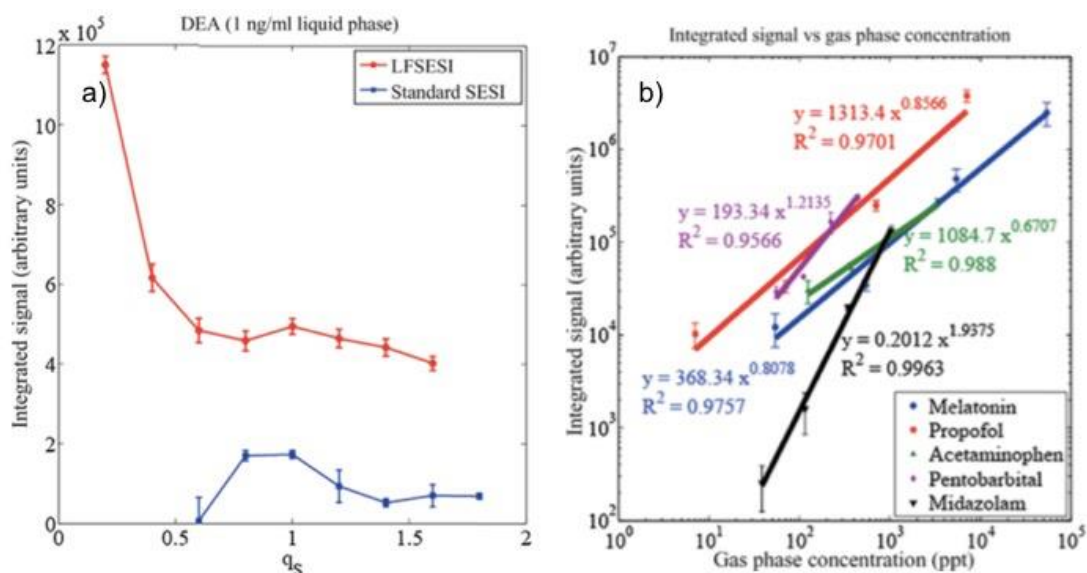
Figure 11 a) Experimental performance of the optimized LFSESI vs the classical (standard) SESI; b) detection of several drug of interest ionized with the optimized LFSESI.

5.3. Conclusions

A numerical model for SESI was developed, which features a numeric electrospray model based purely on electrostatics which gives reasonably accurate results. This model allowed calculating the ionization of vapors by an electrospray cloud in a matter of minutes. The analysis of the concentration distribution of species involved in SESI dynamics revealed that the commonly accepted of constant concentration of neutral vapors due the low probability of ionization is not valid when the sample flow is too low. In this situation, ionized vapors are driven too fast by electric fields to be replaced by new fresh neutral molecules, which result in a loss of neutral vapors in the core of the ionization region. This effect causes ionization efficiency to be lower than the theoretically expected at very low sample flows. Based on the numerical model, an optimized ionizer was designed, which outperformed preexisting SESI-MS performance by a factor of five in terms of ionization efficiency. Some examples on the detection of drugs were provided, suggesting that such system can be suitable for real-time pharmacokinetic studies.

6. Part II. TMIMS: geometry optimization

The second part of this PhD Thesis focuses on the development of numerical simulation tools to understand and optimize TMIMS. This algorithm was motivated by the need of obtain quantitative information about TMIMS performance. Previously, a theoretical model had qualitatively matched TMIMS experimental results. However, it was based on uniform electric fields and did not consider geometry effects. The core of this research discusses the importance of different phenomena, in order to simplify the formulation. The developed algorithm is executed to optimize the TMIMS geometry through parametric sweeps. The results were published in the follow scientific paper:

- Barrios-Collado, C.; Vidal-de-Miguel, G. Numerical algorithm for the accurate evaluation of ion beams in transversal modulation ion mobility spectrometry: Understanding realistic geometries. *Int. J. Mass Spectrometry* **2015**, 376, 97–105

6.1. Methods

Considering the experimental conditions in [30], it is assumable that the movement of ions has no effect on the movement of the gas. The space charge effect in those conditions (ionic currents on the order of *10 pA*) on TMIMS performance can also be considered negligible.

In TMIMS the effect of the gas can be neglected in the majority of the domain. Only at the outlet, the gas velocity field effects are important. Inside the slit, the electric field is shielded and the ions are primarily pushed by the gas flow. The outlet region can be divided into three zones (Figure 12): Zone I, where the ions are primarily driven by electric field and the gas is accelerated toward the slit; Zone II, where electrostatics and fluid velocity co-dominate; and Zone III, where the fluid velocity dominates. Due to the symmetry of the configuration and the zero divergences of the electric field and the fluid velocity field, it can be assumed that only a stream tube passes through the slit with a width of $\delta/l \sim q/(ZEl) \sim 10^{-3}$, where q is the volumetric flow of gas per unit of slit length that is outputted through the slit, Z is the mobility of the ions, and E is the electric field strength in Zone I, which can be assumed to be locally uniform.
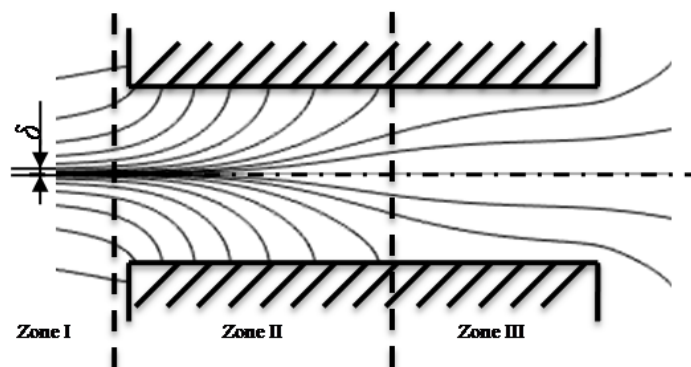
Figure 12 Schematic configuration of the outlet slit

It is hypothesized that δ is known and that all ions in this stream tube in Zone I are transferred. Because Zone I is dominated by the electric field, the fluid velocity field does not need to be simulated. Then, the problem can be formulated as (9),

$$\begin{cases} \dfrac{\partial n}{\partial t} + \nabla \cdot (-Z(\nabla V)n) = Z\dfrac{k_B T}{e}\nabla^2 n \\ \nabla^2 V = 0 \end{cases} \qquad (9)$$

where t is time, n is the volumetric concentration of the ions, V is the electrostatic potential, Z is the mobility of the ions, and Einstein's relation states that the diffusivity D is related with its electrical mobility through the expression $D = Zk_B T/e$. The boundary conditions are: $n = n_0$ at the inlet slit, $n = 0$ at the surfaces of all electrodes, $V = V_0/2$ at the inlet electrode, $V = -V_0/2$ at the outlet electrode, $V = V_{pp}/2w(2\pi f t)$ at the deflector electrode 1, and $V = -V_{pp}/2w(2\pi f t)$ at the deflector electrode 2, where $w(x)$ is an arbitrary periodic function (with unit amplitude), f is the frequency of operation of the TMIMS, and V_0 and V_{pp} are the axial voltage and the peak-to-peak voltage applied to the TMIMS, respectively. The initial conditions are: $n = 0$ at $t = 0$ in the entire domain. According to this formulation, the electric fields can be expressed as a linear combination of steady solutions, which can be easily solved in the entire geometrical domain using common numerical methods. However, the ion concentration distribution requires solving of a non-stationary problem with different scales: the size of the TMIMS cell, the width of the ion beam, and the width of the re-focused beam.

The Péclet number (Pe) of the flow of ions, which compares the convective velocities with the diffusive velocities is $Pe = V_0 e/(k_B T) = 4\cdot 10^5$. This large Pe implies that diffusion broadening of the ion beam (δ_D) is substantially smaller than l and that the curvature of the ion beam, which also scales with l, has a minimal effect on the diffusion process. So, convective effects will dominate the trajectories of the ions. However, although the effect of diffusion is minimal, it cannot be neglected because it is the main limiting factor for the resolving power of the TMIMS. As a solution, it was assumed (i) that the ions would follow an averaged trajectory purely convective, becoming an ordinary differential equation (ODE), which could be directly integrated; and (ii) that diffusion would spread the ions perpendicularly to the mean trajectory in a manner that is equivalent to the trajectory that is produced in an infinitesimally thin ion beam in a steady and uniform field for which an analytical solution exists (10)(11):

$$n \propto \frac{1}{\sqrt{2\pi\sigma_d}}\exp\left(-\frac{1}{2}\left(\frac{y}{\sigma_d}\right)^2\right) \qquad (10)$$

$$\sigma_d = \sqrt{2\frac{Zk_B T}{e}t_r} \qquad (11)$$

where y represents the distance to the center of the beam in the section of interest, n is the concentration of ions, and t_r is the time of residence. The mean trajectories were integrated by considering only the convective transport and assuming that all ions departed from the same point. This integration provided the coordinate (Y) of the ion beam as it reaches the outlet electrode. As illustrated in Figure 13, the instantaneous ion concentration profile that reaches the outlet electrode was estimated by applying (10).
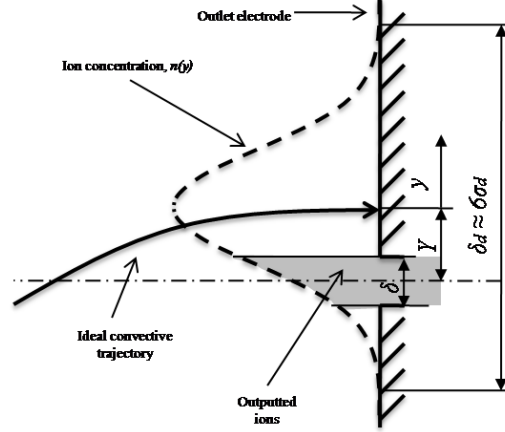
Figure 13 Scheme of the diffusional model and the instantaneous signal

Applying the Buckingham Pi theorem, l, Z and V_0 were used as independent variables, and the problem was reformulated the problem, with the following dimensionless groups: $\lambda = L/l$, $\rho = d/l$, $\tau = tZV_0/l^2$, $\omega = fl^2/(ZV_0)$, $\varepsilon = V_{pp}/V_0$, $Pe = eV_0/(k_BT)$, $w(2\pi\omega\tau)$ and $\tilde{\delta} = \delta/l$.

The algorithm has three main steps: in the first step, the dimensionless electric potentials ($v = V/V_0$) were calculated as $v = v_0 + \varepsilon v_1 w(2\pi\omega\tau)$, which are defined as: $\nabla^2 v_0 = 0$, with boundary conditions $v_0 = \{0.5, -0.5, 0, 0\}$ at the inlet, outlet and both deflector electrodes; and $\nabla^2 v_1 = 0$, with boundary conditions $v_1 = \{0, 0, 0.5, -0.5\}$ at both axial, the first and second deflector electrode.

In the second step, a set of ideal trajectories were integrated (ODE: $dX/d\tau = -grad(v(X,\tau))$, with the initial conditions: $X_0 = (-0.5,0)$). at the initial times $\tau_0 = \{0, 1/(N\omega), 2/(N\omega),...,(N-1)/(N\omega)\}$ (where N is the number of computed trajectories). These computations provided the coordinate of the landing point ($\tilde{Y} = Y/l$) and the time of residence of each ion (τ_r).

In the third step, the instantaneous signal (s) was calculated by integrating the concentration profile along the outputted streamline (12),

$$s(\tau) = \int_{\tilde{Y}(x)-\frac{\tilde{\delta}}{2}}^{\tilde{Y}(x)+\frac{\tilde{\delta}}{2}} \sqrt{\frac{Pe}{4\pi\tau_r(\tau)}}e^{-\frac{y^2 Pe}{4\tau_r(\tau)}}dy \qquad (12)$$

The mean signal outputted by the TMIMS (S) for a given operation conditions and for a given mobility was estimated as $S=\int s(\tau)d\tau$. Each of these calculations provided the signal (S) for a given frequency of operation (ω), geometry (λ, ρ), wave shape (w), voltages (Pe and ε), and flow rate ($\tilde{\delta}$). The spectra were obtained by repeating this process for different values of ω. The electrostatic fields were calculated by two different methods: finite element method (FEM), through COMSOL Multiphysics, and boundary element method (BEM), through Mathworks MATLAB. The convective trajectories were integrated by two regular methods: Runge–Kutta (4,5) and Adams–Bashforth–Moulton.

6.2. Results

The algorithm was executed for the same configuration of the experimental system [30]. To evaluate the convective model, the function $\tilde{Y}(\tau)$ was plotted at the frequency where the function $S(\omega)$ achieved its maximum. As expected, when the ions were not refocused, $\tilde{Y}(\tau)$ showed a periodic pattern with frequency ω. If the focus were perfect, the effective value of $\tilde{Y}(\tau)$ should be zero at the exact maximum. However, as Figure 14 shows, there was a ripple of frequency 3ω, which could not be eliminated. The consistency of these results suggested that this aberration was inherent to the simulated physics and not a numerical effect. To verify that point, the same methods were run with a different set of boundary conditions which produced uniform electric fields, so the aberration should be zero. For these particular boundaries, the root mean square (RMS) of $\tilde{Y}(\tau)$ was on the order of 10^{-5}, whereas the ripple produced with the more realistic conditions was 10^{-4}. As the dimensionless diffusion broadening ($\tilde{\sigma}_d$) is on the order of 10^{-3}, the aberration was considered negligible. The combination of BEM with Runge–Kutta-(4,5) was selected because it provided rapid computations.
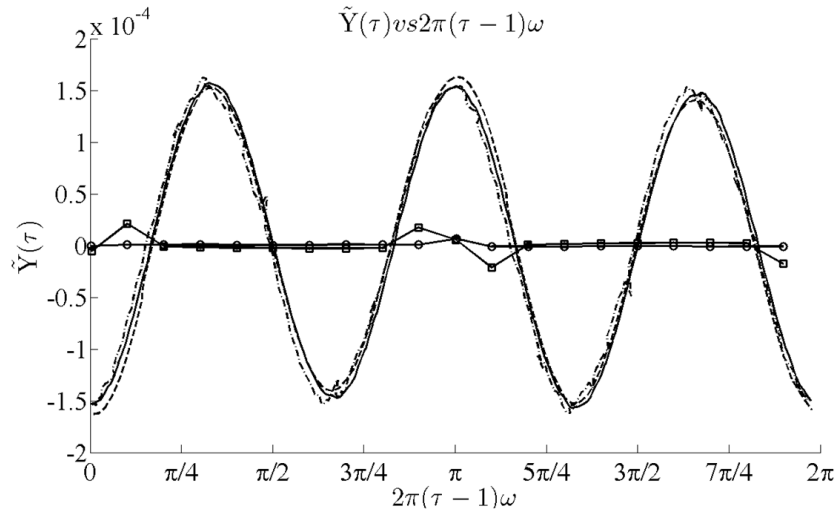
Figure 14 $\tilde{Y}(\tau)$ **at resonant frequency. Circles: analytic uniform fields+Runge–Kutta (4,5); squares: boundary conditions that produce uniform fields, FEM+Runge–Kutta (4,5); solid line: realistic geometry FEM+Runge–Kutta (4,5); dashed line: realistic geometry BEM + Runge–Kutta (4,5); dotted line: realistic geometry FEM + Adams–Bashforth–Moulton**

The spectrum shapes simulated and the experimental [30] were compared. Figure 15a details the experimentally acquired spectrum (circles), which was normalized with the maximum intensity of the peak, and the simulated spectrum (line). Figure 15b shows a parametric study in which the resolving power was evaluated as a function of the ratio between the deflection voltage and the axial voltage ε. This figure shows that the experimental data and the simulations follow very similar trends: linear growth followed by a drop at a maximum resolving power between *50* and *60*. The measured and the numerically predicted optimum values are in a reasonably good agreement. The computational optimum is at $\varepsilon = 1.7$, while the experimental one is at $\varepsilon = 1.76$. It also explains why the resolving power falls above this optimum: for values of ε greater than the optimum, ions begin to collide with the deflector electrodes. The maximum resolving power was only overestimated with an error of *10.5%*.
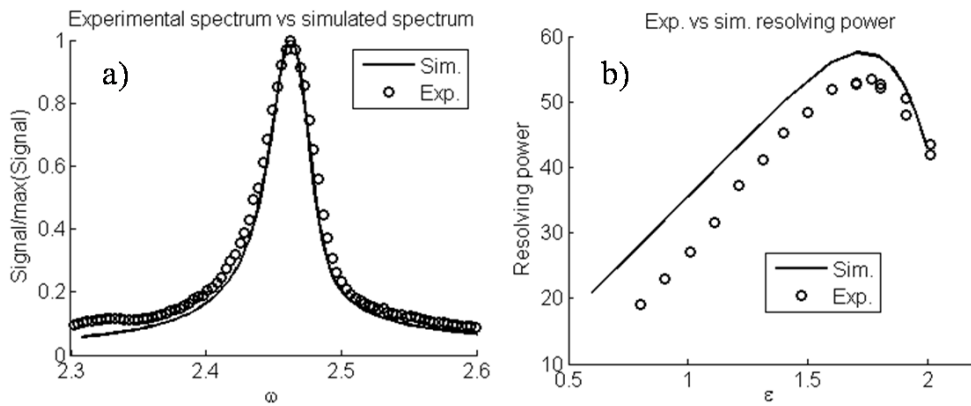
Figure 15 a) Experimental vs simulated spectra; b) resolving power vs ε
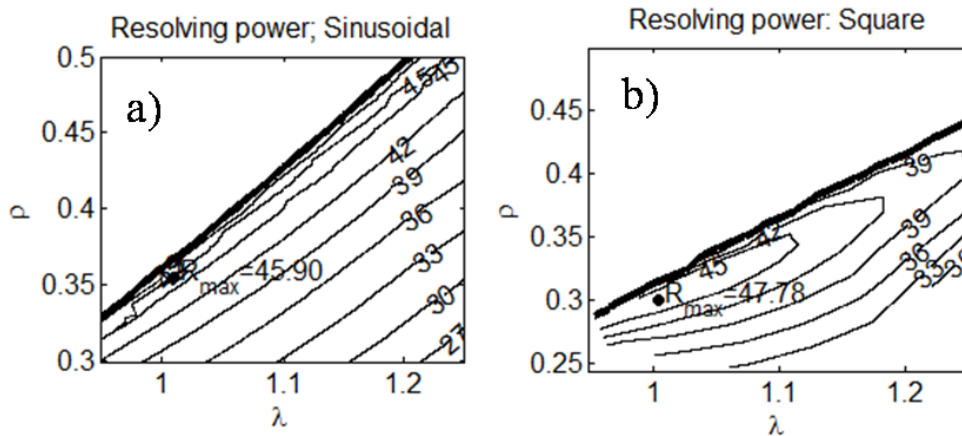
Figure 16 Resolving power contour maps: a) sinusoidal wave; b) square wave

Figure 16 represents the numerically estimated resolving power as a function of the geometry parameters, for two different types of wave shapes, and with $\varepsilon = 1$, $Pe = 3.1 \cdot 10^5$, and $\tilde{\delta} = 10^{-3}$. For an optimized geometry, the maximum power achieved with a sinusoidal wave (Figure 16a) was $R = 46$, for an optimized geometry with $\lambda = 1.03$ and $\rho = 0.37$. For the square wave (Figure 16b) the maximum resolving power was $R =$

48 with $\lambda = 1.00$ and $\rho = 0.30$. The square wave provides a slightly better resolving power and the frequency can be varied more easily than a sinusoidal wave. In the final section of the study, the effect of finite and realistic rising and falling times is analyzed by means of a fin-shaped wave (13),

$$
w(\tau) = \begin{cases} 1 - \dfrac{2}{1 + e^{-\frac{1}{2\omega\tau_0}}} e^{-\frac{\tau}{\tau_0}}, & 0 \leq \tau < \dfrac{1}{2\omega} \\[4mm] -1 + \dfrac{2}{1 + e^{-\frac{1}{2\omega\tau_0}}} e^{-\frac{\tau - \frac{1}{2\omega}}{\tau_0}}, & \dfrac{1}{2\omega} \leq \tau < \dfrac{1}{\omega} \end{cases} \qquad (13)
$$

where the new parameter τ_0 was employed to consider the characteristic setting times of the rising and the falling edges. The maximum resolving power decreased when τ_0 increased as the wave became 'less square'. According to the results provided by the algorithm, for τ_0 less than *3%* of the wave period the resolving power remained near the ideal. Which for the typical frequencies of operation of the TMIMS (*1 kHz*), the maximum acceptable settling times would be around *30 μs*.

6.3. Conclusions

The results provided by the proposed algorithm are in good agreement with the measured experimental results. Due to its simplicity, the algorithm developed in this study enabled a high-speed evaluation of TMIMS performances. Optimum geometries were obtained by evaluating the resolving power was evaluated on the domain defined by the two geometrical parameters. In addition, the numerical method also revealed that there is an aberration effect, which may limit the maximum achievable resolving power. For the applied voltages, the scale of this phenomenon was one order of magnitude less than the spread produced by diffusion. The algorithm also provided a key requirement for the square wave system, which would be required to power an optimized TMIMS with a resolving power of 48.

7. Part III. TMIMS: space charge

The third part of this PhD Thesis is a follow-up of the TMIMS geometry optimization. The previous algorithm reproduced the TMIMS tune-up routine, which was enough to optimize geometry. Space charge was not considered as it was demonstrated that, in those particular conditions, it is negligible. However, in real conditions, it is not unusual that the analyte of interest is hidden inside a complex cloud of irrelevant ions, whose space charge effect can downgrade performance. In this research, a simple approximation of this situation is proposed. The results are to be published in the follow scientific paper:

- Barrios-Collado, C.; Vidal-de-Miguel, G. A numerical model of the influence of high concentration, small collision cross section species on trace concentration, and high collision cross section target analytes in Transversal Modulation Ion Mobility Spectrometry (TMIMS) (under review).

7.1. Methods

The input ion mixture in the TMIMS typically contains a high concentration of low molecular weight ions. These are small collision cross section species. However, high molecular weight ions or higher collision cross section macromolecules are more pertinent for these types of analyses. For example, buffer ions such as H_3O^+ have mobilities around *2 $cm^2/V/s$*. In contrast, the mobilities, as measured by TMIMS of proteins [79] are in the order of *1 $cm^2/V/s$* or less. A simple model of two species interacting in TMIMS was considered. Species b (with mobility Z_b) signifies the buffer ion, which is abundant and is not transmitted. Meanwhile, species t (with mobility Z_t) signifies the target ion. This ion is found at a low concentration and moves more slowly than species b ($Z_b > Z_t$).

The target ion was assumed to be at a very low concentration, as previously described [88], so its contribution to the electric fields is negligible compared to the contributions of the electrodes or the buffer species. Then, all space charge effects were attributed to the buffer ion. By decoupling the simulation of the buffer beam from the target beam and allowing the space charge effects on the target beam to be calculated as an additional electric field, this hypothesis simplifies the numerical model.

When considering a planar buffer beam of charge density σ_{sc}, the electric field is on the order of $E_{sc} \sim \sigma_{sc}/(2\varepsilon_0)$, where ε_0 is the vacuum permittivity. Assuming a time of residence of $t_r \sim l^2/Z_b/V_0$, (where l and V_0 are the TMIMS length and the axial voltage) an ion current I, and a beam surface A, σ_{sc} is on the order of $\sigma_{sc} \sim Il^2/(Z_bV_0A)$. Then, the cumulative displacement caused by space charge d_{sc} during t_r, is on the order of $d_{sc} \sim Z_bE_{sc}t_r \sim Il^3/(2\varepsilon_0V_0^2A)$, which for a *$V_0 = 8$ kV, $l = 5$ cm, $A = 5$ cm^2* [88] and *$I = 1$ nA* is on the order of *$d_{sc} \sim 2.2\cdot10^{-5}$ cm*. In contrast, the convective, displacement is on the order of l, which is around *$2.3\cdot10^5$* times larger than d_{sc}. As discussed in [88], diffusion is negligible against convection, as the Péclet number is in the order of *$3.1\cdot10^5$*. This means that the effects of space charge and diffusive broadening are on the same order.

So, the displacements caused by space charge and diffusion do not affect significantly the position of the buffer beam, although, as seen in [88], their effect is crucial on the spectra shape, and thus, on performance. However, as performance was not evaluated for the buffer ion, both effects were not considered. This hypothesis reduces the buffer beam to the centerline defined by the convective displacement, which concentrates all the electrical charge.

The hypothesis formerly described allowed to build a computational method which can be described, in a nutshell, as follows: 1) simulation of the buffer ion convective trajectories using the non-space-charge model; 2) reconstruction of the buffer ion beam centerline using its purely convective trajectories and assigning the space charge distribution, which depends on the ionic current; 3) simulation of the target beam adding a perturbation term that represents the space charge effect; and 4) application of the diffusion model and reconstruction of the spectrum as described in [88]. The whole process was repeated varying the mobility of the buffer ion and the ionic current. The algorithm was built dimensionless, in a similar fashion of [88]. Two new variables were included: the mobility ratio Z_b/Z_t and the dimensionless ionic current I/I_{ref}. I_{ref} is defined as the ionic current whose space charge perturbation over the target ion trajectories is in the same order of TMIMS convective displacements ($I_{ref} = qV_0\varepsilon_0/l^2$, were q, V_0, ε_0 and l are the volumetric flow, the axial voltage, the vacuum permittivity and the TMIMS length respectively).

The space charge distribution was assigned to a region in the space that encompasses the buffer beam. Therefore, from the point of view of the target species, the buffer beam behaved as a "fifth electrode" which caused a perturbation that diverts the target beam. For practical reasons, the buffer beam was considered to be a planar ion beam with constant surface charge density. Its thickness was reduced to its centerline in the TMIMS domain. The beam was reconstructed for each instant by interpolation of the calculated buffer ion trajectories and was spatially discretized. Every node was assigned a surface charge density approximated by $\sigma_{sc} = Il^2/(Z_bV_0A)$, where σ_{sc}, I, Z_b, V_0, l, and A are the nodal space charge surface density, the ion current, the buffer mobility, the axial voltage, the length of the TMIMS, and the area of the planar ion beam respectively. The charge distribution along the ion beam followed a piecewise linear distribution, previously described [88]. The dimensionless voltage (v_{sc}) and electric field originating from the buffer ion beam could then be calculated anywhere along on the TMIMS domain using analytical expressions.

In addition, in TMIMS, the electrodes are kept at their operating voltage by the power supplies. Therefore, the superimposed electric potentials on an electrode are equal to the electrode working voltage, so there must be a "reaction", v_r, which compensates the effect of v_{sc} on the electrodes. v_r was calculated by means of the Laplace equation ($\nabla^2 v_r = 0$) was used with boundary conditions $v_r = - v_{sc}$ on all electrode surfaces.

Therefore, in the target ion simulation, the incorporation of the buffer ion space charge effects is reduced to two additional terms, which represent the perturbation. This inclusion was modeled without carrying out a spatial discretization of the whole domain. Z_b/Z_t and I/I_{ref} were swept in order to obtain a large dataset of spectra. The rest of the parameters were tuned according to the optimization results obtained in [88]. The algorithm works similarly to what has previously been described [88]. The electrostatic fields were computed using the Boundary Element Method (BEM). The ion trajectories were integrated via the Adams-Bashforth-Moulton method. The entire method was programmed using the Mathworks MATLAB software package.

7.2. Results

Figure 17 shows an example ($Z_b/Z_t = 2$, $I/I_{ref} = 1$) of the electric potential along with the buffer ion beam. The black isopotential lines represent the dimensionless ideal voltage in the absence of the space charge v), while the colored regions represent the dimensionless perturbation field $v_{sc} + v_r$. This perturbation not only affects the area that is proximal to the buffer beam, but also covers a significant part of the TMIMS domain. At $Z_b/Z_t > 1.1$, the buffer beam hits the deflector electrodes. Therefore, the method was designed to recognize when the ion beam hits the deflector electrodes and splits into two segments.
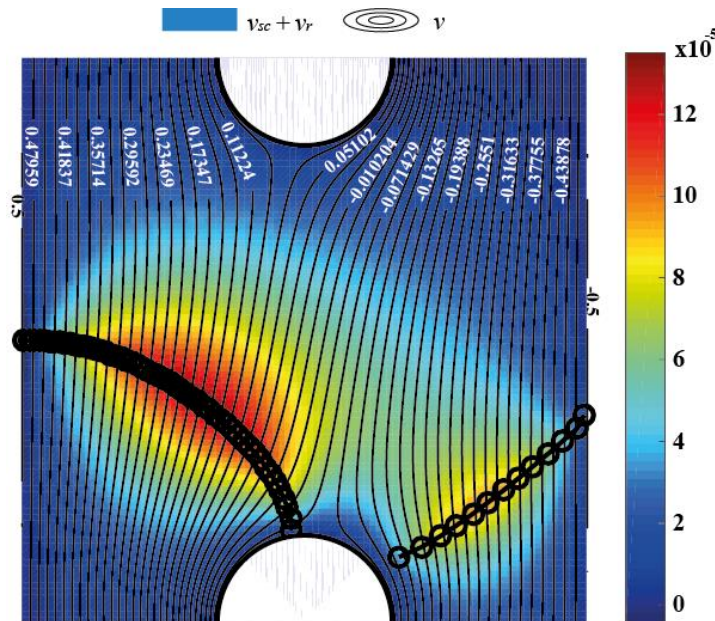
Figure 17 Space charge perturbation field (Z_b/Z_t= 2, I/I_{ref} = 1)

The results demonstrate that the space charge effects have a negative effect on the performance of TMIMS. The resonant frequency shifts. The signal and resolving power decrease. The algorithm does not appear to be reliable at very low mobility ratios ($Z_b/Z_t < 1.2$). Likely, this is because of numerical instabilities that are a consequence of mathematical singularities. From $Z_b/Z_t = 1.2$ and up, the algorithm is robust and covers the expected range of mobilities observed in real experiments. Increasing the term I/I_{ref} degrades the peak shape to the point at which there is a critical I/I_{ref} where the

performance evaluation no longer makes sense. This is the maximum current TMIMS can handle. Figure 18 shows several spectra for a fixed mobility ratio ($Z_b/Z_t = 1.25$) and several buffer ion currents. The critical I/I_{ref} is deduced through visual inspection of spectra for each Z_b/Z_t. Regarding Z_b/Z_t, changes in performance are significant at low mobility ratios. Meanwhile, at high Z_b/Z_t there are virtually no effects on the target ions. In the worst-case scenario of $Z_b/Z_t = 1.2$, which the minimum mobility ratio that the algorithm can handle, the critical current is around $I/I_{ref} \sim 10$. For a TMIMS with $V_0 = 8$ kV, $l = 5$ cm, and $q = 1$ lpm, this results in $I \sim 5$ nA.
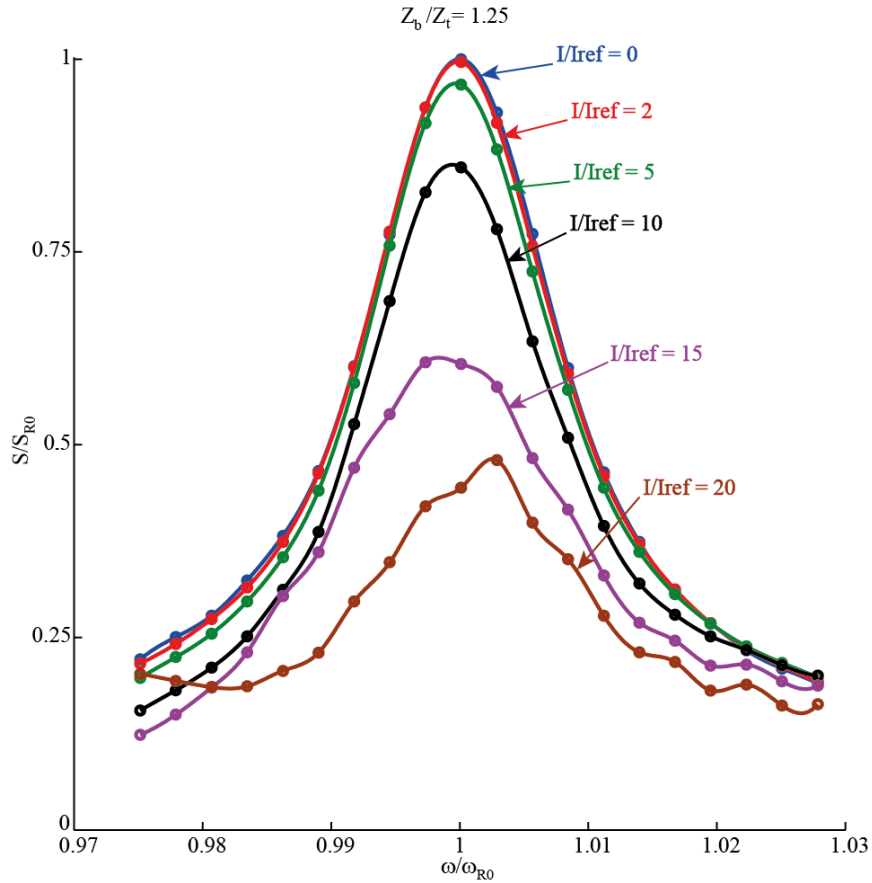
Figure 18 Degradation of spectra ($Z_b/Z_t = 1.25$)

The changes in performance were evaluated by comparing the resonant frequency, the signal at resonant frequency, and the resolving power under this case without considering space charge ($I/I_{ref} = 0$). In general, performance worsens with higher I/I_{ref}, however, at high Z_b/Z_t, changes in performance are negligible. The results were fit to semi-empirical expressions (Figure 19). First, the performance characteristics were fitted versus I/I_{ref} for each Z_b/Z_t. Then, the parameters of these fittings were fitted versus Z_b/Z_t. With fixed mobility ratios and variable ion currents, the resonant frequency shifts linearly. The peak signal drops quadratically and the resolving power changes according to a cubic expression. The parameters of these expressions follow rational functions that include mobility ratios. These functions tend asymptotically towards zero at high mobility ratios while diverging towards the unitary mobility ratio.

36

a)

b)
$$\frac{\omega_R}{\omega_{R0}} - 1 = \frac{I}{I_{ref}} A$$

$$A = \frac{\frac{Z_b}{Z_t} 7.388 - 9.5}{\left(\frac{Z_b}{Z_t}\right)^2 - \frac{Z_b}{Z_t} 1.894 + 1.315} \cdot 10^{-4}$$

c)

d)
$$\frac{S}{S_0} = \left(\frac{I}{I_{ref}}\right)^2 B + 1$$

$$B = \frac{-9.322 \cdot 10^{-5}}{\left(\frac{Z_b}{Z_t}\right)^3 - \left(\frac{Z_b}{Z_t}\right)^2 4.001 + \frac{Z_b}{Z_t} 5.514 - 2.525}$$

e)

f)
$$\frac{R}{R_0} = \left(\frac{I}{I_{ref}}\right)^3 a + \left(\frac{I}{I_{ref}}\right)^2 b + 1$$

$$a = \frac{-4.41 \cdot 10^{-6}}{\left(\frac{Z_b}{Z_t}\right)^2 - \frac{Z_b}{Z_t} 2.518 + 1.627}$$

$$b = \frac{4.41 \cdot 10^{-5}}{\frac{Z_b}{Z_t} - 1.27}$$
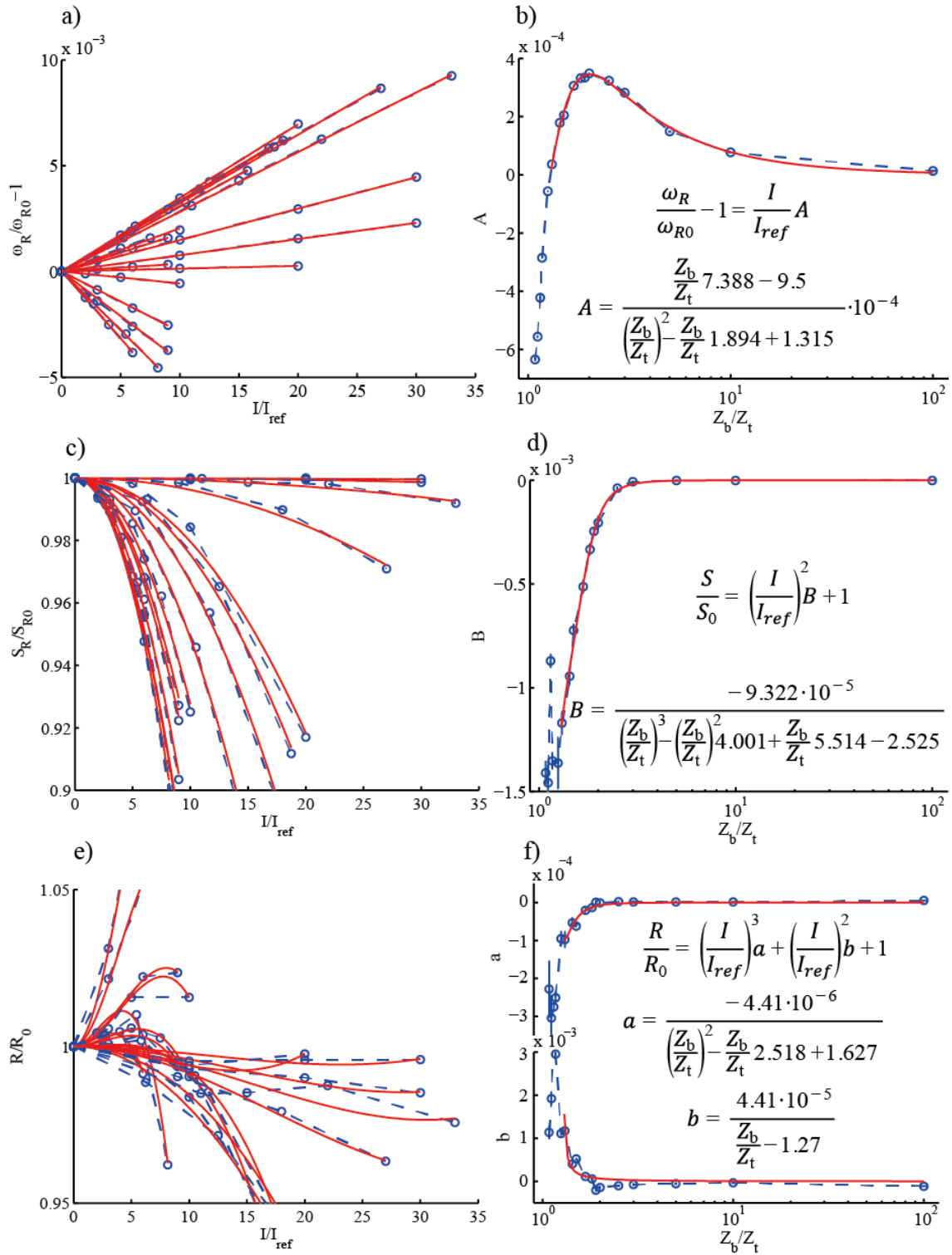
Figure 19 Performance changes caused by space charge in the main performance characteristics: a), b) Resonant frequency; c), d) Signal at resonant frequency; e), f) Resolving power.

37

7.3. Conclusions

Space charge effects produce a general loss of performance in TMIMS devices by displacing the frequency of resonance and lowering transmission and resolving power. This outcome is a result of deviations in the target ion convective paths. These deviations are caused by the buffer ion beam space charge electric field.

The proposed numerical method shows signs of instability when the mobility ratio tends to be unitary, regardless of the strength of the ionic current. This is mainly due to the appearance of mathematical singularities. However, when the mobility of the buffer ion is 20% higher or more than the mobility of target ion, the algorithm becomes robust. This is the expected range of mobilities in real experiments.

The spectra degraded when the ion current was increased to the cutoff value. At this point, the spectra are so degraded that they become unrecognizable. This critical current increases as a function of the mobility ratio. In the worst-case scenario, when the buffer mobility is close to the target mobility, this cutoff value of the current is in the order of a few nanoamperes. With fixed mobility ratios and variable ion currents, the resonant frequency shifts linearly. The peak signal drops quadratically and the resolving power changes according to a cubic expression. The parameters of these expressions follow rational functions that include mobility ratios. These functions tend asymptotically towards zero at high mobility ratios while diverging towards the unitary mobility ratio.

8. Part IV. Testing in a relevant environment

The fourth and final part of this PhD thesis represents a test on a relevant environment of the proposed vapor analyzer. A plant (*Begonia semperflorens*) metabolism is described by analyzed the volatile organic compounds (VOCs) released from the own plant. The results were published in the follow scientific paper:

- <u>Barrios-Collado, C.</u>; García-Gómez, D.; Zenobi, R.; Vidal-de-Miguel, G.; Ibáñez, A. J.; Martínez-Lozano Sinues, P. Capturing in vivo plant metabolism by real-time analysis of low to high molecular weight volatiles *Anal Chem* **2016** 88(4):2406-12

8.1. Methods

The plant, (*Begonia semperflorens*) was enclosed inside a glass chamber which featured an inlet for humid, compressed air and an outlet connected to the LFSESI, which was coupled to a Thermo-Fisher LTQ Orbitrap mass spectrometer. Figure 20 shows a picture and a diagram of the setup.
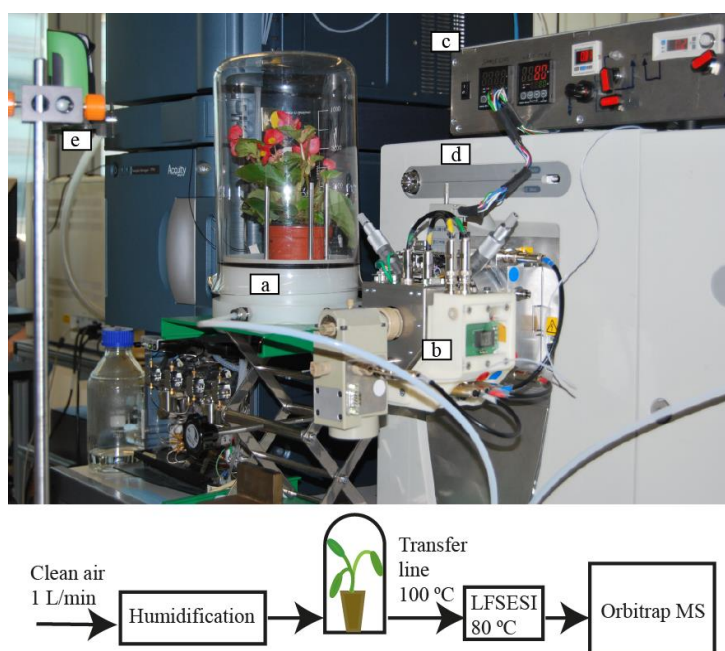
Figure 20 Experimental set-up: (a) glass beaker containing the plant; (b) SESI source; (c) SESI control module; (d) Orbitrap MS; (e) time- lapse camera

Two different experiments were run: (i) light-induced emitted VOCs and (ii) VOCs emitted by the plant under stress due to mechanical damage. In the former case, the plant was measured nonstop during 3 entire days. In the response under stress experiment, the plant was measured under normal conditions during 90 min to establish the baseline. The chamber was then opened and the upper leaves were pierced. The response of the plant was then recorded during 120 min. In addition, some key compounds observed in the experiments were identified by performing MS/MS in real time and comparing the fragmentation with standards.

During a three-day nonstop measurement, VOCs with a clear correlation with the light levels in the room were noticed. The mass spectra contained more than *3000* resolved peaks (after filtering isotopes) in the range of *50−500 Da*, which were subjected to hierarchical cluster analysis. Four distinct trends were identified: (1) compounds whose intensity showed almost no change during the three-day experiment; (2) those which showed a decreasing trend without day−night correlation; (3) compounds with a constant rising trend; and (4) those with a clear periodic pattern correlated with the day−night cycle. Compounds of trends 1 and 2 (around *86%* of all mass spectral features) were chemical noise not related with the "plant ecosystem" (defined as the plant and the soil), whereas the third (*85* mass spectral features) and fourth (*156* mass spectral features) trends were associated with the plant ecosystem. Of those showing a periodic fluctuation, *111* were diurnal species (i.e., maximum emission rates were around midday) and *55* were nocturnal species (i.e., maximum emission rates were around midnight). Figure 21 shows the heatmaps corresponding to the diurnal and nocturnal species, respectively. Further visual inspection of the time traces revealed *154* additional compounds which were the sum of a periodic pattern and a decreasing negative-exponential baseline as the emission rates did not reach the steady state in three days. In a similar fashion, *74* additional nocturnal substances were identified.
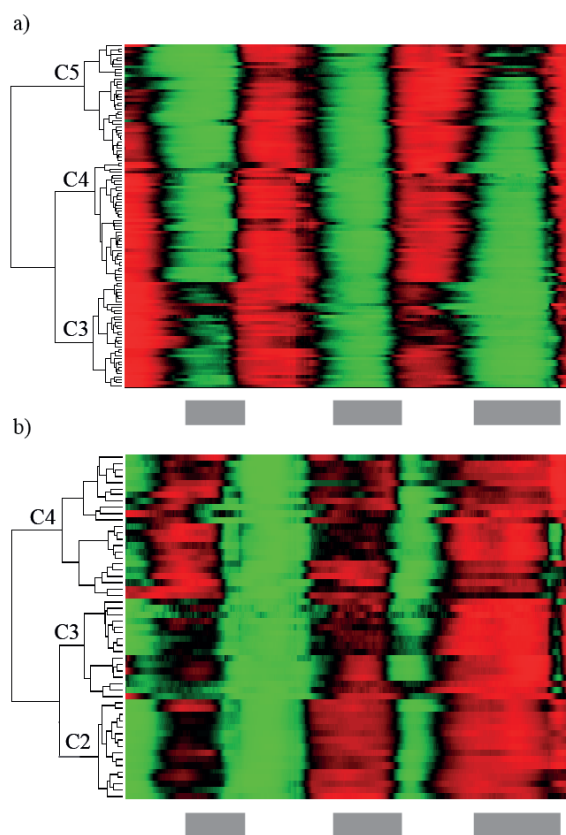
Figure 21 Heatmaps of diurnal (a) and nocturnal (b) emissions

In order to validate these observations, a targeted approach was performed, focusing on key compounds universally found on plant VOCs, such as monoterpenes (*m/z 137.1324*) and sesquiterpenes (*m/z 205.1950*) which are two families of metabolites related to photosynthesis [89]. Figure 22 shows the mass spectrum in the region at *m/z 137*. It shows four clearly resolved peaks separated by less than *0.1 Da* (*m/z 137.0248, 137.0596, 137.0958*, and *137.1324*). The latter corresponds to the monoterpene family $[C_{10}H_{17}]^+$. The inset shows the corresponding time traces for each of the peaks. As expected, the monoterpenes show a periodic diurnal behavior. The most abundant compound at *m/z 137.0958* $[C_9H_{13}O]^+$ showed a sort of periodic pattern with an accumulation tendency during the three days. In contrast, the two minor species at *m/z 137.0248* and *137.0596* showed a flat or falling tendency, indicating that they were just chemical noise not related to the plant ecosystem. This example illustrates the importance of using high-resolution mass analyzers for real-time analysis of complex mixtures. For comparison, Figure 22 along with the experimental mass spectrum, shows the simulated spectrum at resolution *3000* for these four species (the typical resolution of a high-end state-of-the-art system [12]). Clearly, at this resolving power, the four species would have gone unresolved and the identification and quantification of the monoterpenes would have been seriously compromised.
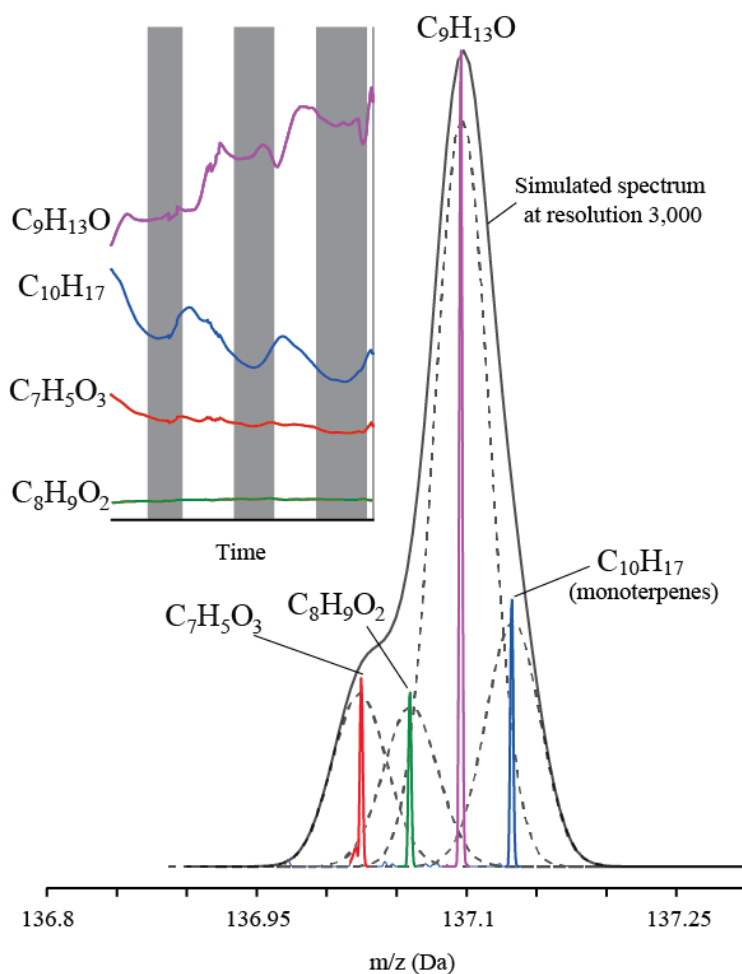
Figure 22 Mass spectrum at *m/z 137*

Figure 23a shows two examples of compounds whose emissions were oppositely correlated with the day−night cycle. The first species peaked around 8:30−9:00 a.m. to then decline until it reached a minimum around 1 a.m., when it bounced back to recover again the previous day's levels. In contrast, the second example shown in Figure 23a has a maximum around 1 a.m. and its levels drop until 8−9 a.m., when it reaches a minimum. In this case, although the period pattern is clearly preserved across the three days, it shows an accumulation trend. This results in highest concentration values during the third night. In addition, the profile shows a plateau, rather than a well-defined maximum (as the diurnal compound), suggesting different kinetics. The diurnal compound was identified as β-caryophyllene (Figure 23b). β-Caryophyllene is one of the most important sesquiterpenes, which is directly related to photosynthesis [90]. The nocturnal compound has been assigned to indole based on its accurate mass and isotopic distribution. Indole is usually related to plant defense against herbivore attack [91] and is also used as an inhibitor for the germination of seeds of other plant species [92].
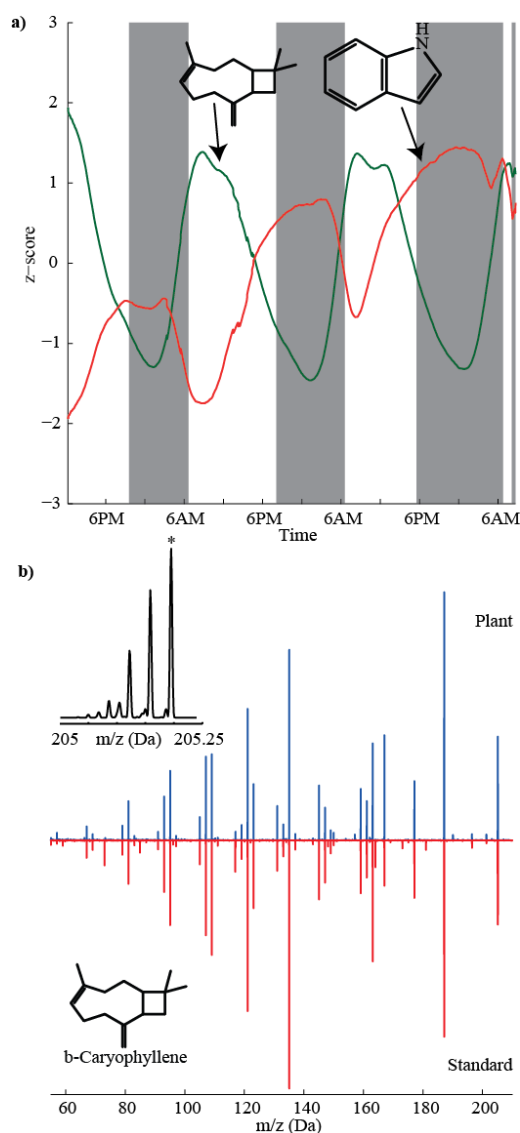
Figure 23 a) Time traces for β-caryophyllene (green) and indole (red); b) MS/MS confirmation of β-caryophyllene

In order to further illustrate the potential of our vapor analyzer to study plant metabolism, the plant was subjected to a stress event and its response was examined. First, the plant was monitored around 1.5 h under normal conditions. Then, some upper leafs were pierced (i.e., mimicking an insect attack event), and the plant's instantaneous response was observed during 2 h after wounding the leaves. Because of the mechanical damage, there was a rise in the emission of *1224* compounds. Interestingly, *996* of them were not previously detected in the three-days experiment. This suggests that this wide range of molecules was associated with stress-induced metabolism Figure 24 shows the heatmap of the *1224* species whose emission rose upon leaf piercing, providing an overview of the plant response. The kinetics were similar for all the species, but with some subtle differences. Figure 25a displays five selected examples. Two of them were identified by MS/MS as methyl jasmonate and hexenyl acetate (Figure 25b). The third one is a sesquiterpene or probably a mixture of them (i.e., isomeric structures), and the rest are two unidentified molecules detected exclusively during mechanical damage. Methyl jasmonate is a chemical alarm for herbivore attack and an insect digestive inhibitor, and (Z)-3- hexenyl acetate is an attractant to predatory insects [93]. Both are related through the oxylipin pathway and rose under stressful conditions, as expected. Their time profiles, as well as the sesquiterpenes, were actually very similar, with a sharp increase during ~8 min to then reach a plateau until min 50, followed by a decline until min 100 and when they recovered again part of the signal during the last 20 min. In contrast, the $[C_7H_{17}O_2]^+$ species rose sharply after the mechanical damage to peak 20 min later. It then constantly declined during 80 min and stabilized during the last 20 min. A totally different behavior was shown by the unknown compound at *m/z 134.0808*, which increased constantly during the 2 h following the leaves piercing. Such distinct behavior and rapid changes in VOCs profiles illustrate the benefit of using real-time techniques to capture such events with enough time resolution.
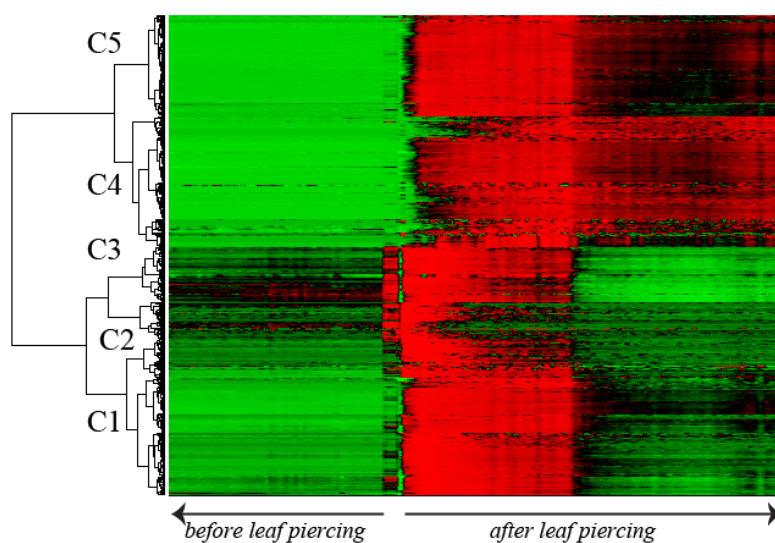
Figure 24 Heatmap of plant response to mechanical damage
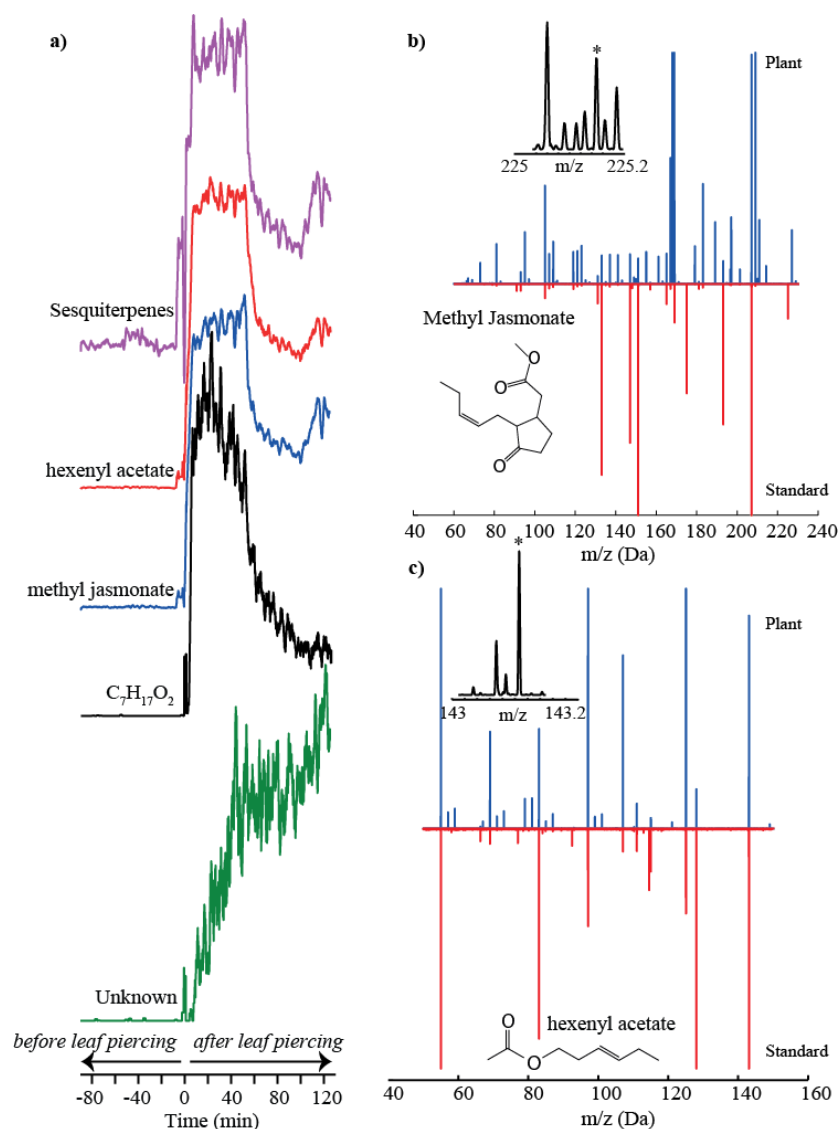
Figure 25 a) Different VOCs kinetics as response to mechanical damage; b) and c) MS/MS confirmation of methyl jasmonate and (Z)-3-hexenyl acetate

8.3. Conclusions

In conclusion, this analytical platform is able to detect hundreds of VOCs covering typical GC/MS methods range (i.e., *50−500 Da*), in real time and without sample preparation. Around *400* species were found to correlate with light levels (i.e., diurnal and nocturnal). Some of these species were identified by MS/MS and confirmed an overlap between the species typically investigated by GC/MS and the VOCs detected by SESI-MS. More than *1200* VOCs emitted by the plant were detected as result of mechanical damage, with a large overlap with compounds described in the literature. However, we observed significant VOC changes on the time scale of minutes, implying that these details would have gone undetected by off-line methods without the required sampling frequency. SESI-MS could provide valuable complementary real-time chemical information on plant metabolomics to GC/MS, which in addition is still indispensable for accurate chemical identification isomeric species.

9. General conclusions

The main conclusions of this PhD Thesis are the following:

- A numerical simulation tool of SESI technique was developed. The results served to design an optimized SESI ionizer which quintuplicates preexisting SESI-MS performance. The highlight of this computational tool was the implementation of the electrospray numerical model.
- The results of the SESI numerical simulations show that the commonly accepted hypothesis of constant concentration of neutral vapors at low probability of ionization is not true. At low sample flows there is a lean concentration of neutral vapors at the ionization region as the ionized vapors are extracted too quickly to be replaced by fresh neutral vapors. As consequence, real ionization efficiency is lower than the theoretical one.
- A numerical model of TMIMS was developed in order to quantitatively study its performance and optimize the geometry. This algorithm was numerically validated through analysis of error convergence, and experimentally validated with literature. As the computational requirements were low, parametric sweeps of geometry parameters were executed to optimize the geometry. The maximum resolving power calculated for a single TMIMS cell was 48, operating with square wave.
- A numerical model of TMIMS was developed to simulate the effect of space charge, which combines two species: a target ion in low concentration and high collision cross section, and an irrelevant buffer ion in high concentration and mobility. This latter produces a space charge perturbation which downgrades TMIMS performance. Semiempirical equations for changes in resonant frequency, maximum peak signal and resolving power were deduced. This algorithm shows signs of instability when the difference of mobilities is lower than 20% of the target mobility. However, it covers the expected mobility range.
- An application in a relevant environment was presented, which consisted in the real-time, in vivo, analysis of a plant metabolism through the volatile organic compounds released from the plant. Hundreds of volatile organic compounds were detected, covering the typical range of GC-MS methods (50-500 Da), although in real-time and without sample preparation. The configuration of the system consisted on the SESI ionizer coupled to a high resolution mass spectrometer. Variations on volatile concentrations in a matter of minutes were noticed, which may be unobserved with GC-MS methods, and key compounds found in literature were detected as a validation of the system. Future developments may include a mobility stage in order to separate isomers, which now is only possible with GC-MS methods.

10. Conclusiones generales

Las principales conclusiones de esta Tesis Doctoral son las siguientes:

- Se ha desarrollado una herramienta de simulación numérica del proceso SESI, mediante la cual ha sido posible diseñar un ionizador SESI optimizado, que quintuplica la sensibilidad de los ionizadores preexistentes. El mayor logro de esta herramienta de simulación numérica ha sido implementar el modelo numérico del electrospray. Los resultados de la simulación numérica del SESI muestran que la hipótesis comúnmente aceptada de que la concentración de vapores neutros es isotrópica a bajas probabilidades de ionizaciónno es del todo correcta. Para bajos caudales de muestra la concentración de vapores neutros se empobrece en la zona de ionización debido a que los iones son extraídos demasiado rápido para ser reemplazados por vapores neutros frescos. Como consecuencia, la eficiencia de ionización real es menor que la teórica.

- Se ha desarrollado un modelo numérico del TMIMS para estudiar cuantitativamente su desempeño y optimizar la geometría. Este algoritmo ha sido validado numéricamente mediante el análisis de la convergencia del error, y experimentalmente comparándolo con estudios en la literatura. Debido a su bajo requerimiento computacional, se ha podido ejecutar la optimización realizando barridos paramétricos de los parámetros geométricos. La resolución máxima calculada de una celda TMIMS ha sido 48, operando con onda cuadrada.

- Se ha desarrollado un modelo numérico del TMIMS para el simular el efecto de la carga espacial que considera dos especies: un ion objetivo en baja concentración y sección eficaz de colisión grande, y una especie no relevante de alta movilidad y alta concentración. Esta última produce un efecto de carga espacial que perjudica las prestaciones del TMIMS. Se han obtenido expresiones semiempíricas de los cambios en la frecuencia de resonancia, señal máxima y resolución. Este algoritmo se muestra inestable cuando la diferencia de movilidades de ambos iones es menor al 20%. Sin embargo, cubre el rango de movilidades esperado.

- Se ha presentado una aplicación práctica del sistema de análisis de gases en un entorno relevante, consistente en analizar el metabolismo de una planta a partir de los compuestos orgánicos volátiles emitidos por una planta en vivo y en tiempo real. Se detectaron cientos de compuestos organovolátiles en el rango típico de los métodos GC-MS (50-500 Da), pero en tiempo real y sin preparación de muestra. La configuración del analizador en este estudio combinó el ionizador SESI con un espectrómetro de masas de alta resolución. Se encontraron variaciones en la emisión de sustancias en cuestión de minutos, que con los métodos GC-MS pasarían desapercibidas, y multitud de compuestos existentes en la literatura como validación del sistema propuesto. En el futuro se podría incluir la etapa de separación por movilidad parar incorporar separación por movilidad de isómeros, hasta ahora sólo posible mediante GC-MS.

11. Contributions

11.1. Publications as first author

- Barrios-Collado, C.; Vidal-de-Miguel, G.; Martínez-Lozano Sinues, P. Numerical Modeling and Experimental Validation of a Universal SESI Source for Mass Spectrometric Gas Analysis in Real-Time. *Sensor Actuat B-Chem* **2016**, 223, 217-225

- Barrios-Collado, C.; Vidal-de-Miguel, G. Numerical algorithm for the accurate evaluation of ion beams in transversal modulation ion mobility spectrometry: Understanding realistic geometries. *Int. J. Mass Spectrometry* **2015**, 376, 97–105

- Barrios-Collado, C.; Vidal-de-Miguel, G. A numerical model of the influence of high concentration, small collision cross section species on trace concentration, and high collision cross section target analytes in Transversal Modulation Ion Mobility Spectrometry (TMIMS) (under revision).

- Barrios-Collado, C.; García-Gómez, D.; Zenobi, R.; Vidal-de-Miguel, G.; Ibáñez, A. J.; Martínez-Lozano Sinues, P. Capturing in vivo plant metabolism by real-time analysis of low to high molecular weight volatiles *Anal Chem* **2016** 88(4):2406-12

11.2. Research stays at prestigious international centers

- 24 months at Professor Renato Zenobi research group at the Laboratory of Organic Chemistry at the Swiss Federal Technology Institute (ETH-Zürich, Zurich, Switzerland). Jan 2014 – Dec 2015.

11.3. Poster presentations at conferences as presenting author

- Barrios-Collado, C.; Zenobi, R.; Vidal-de-Miguel, G. *Towards an Add-on Secondary Electrospray ionizer for pre-existing API-MS and for high sensitivity analysis of volatiles*. 20th IMSC, Geneva (Switzerland), Aug 2014.

- Barrios-Collado, C.; Baertschi, C.; Zenobi, R.; Martínez-Lozano, P.; Vidal-de-Miguel, G. *Add-on Secondary Electrospray Ionizer, delivering high ionization efficiency of vapors for pre-existing API-MS*. Swiss Chemical Society Fall Meeting 2014, Zurich (Switzerland), Sep 2014.

- Barrios-Collado, C.; García-Gómez, D.; Zenobi, R.; Martínez-Lozano Sinues, P.; Vidal-de-Miguel, G. *A Universal Low-Flow Secondary ElectroSpray Ionizer: High Sensitivity Volatile Analysis on Pre-existing MS Instruments*. Swiss Chemical Society Fall Meeting 2015, Lausanne (Switzerland), Sep 2015.

- Barrios-Collado, C.; Schwarz, E.; Dallmann, R.; Li, X.; Bregy, L.; García-Gómez, D.; Brown, S.; Kohler, M.; Zenobi, R.; Vidal-de-Miguel, G.; Martínez-Lozano Sinues, P. *Development of a real-time breath analysis platform and applications: Diagnosis in humans and drug monitoring in mice*. MSACL EU 2015 Salzburg (Austria), Sep 2015.

- Barrios-Collado, C.; García-Gómez, D.; Gaugg, M.; Zenobi, R.; Vidal-de-Miguel, G.; Martínez-Lozano Sinues, P. *Development of a comercial add-on for*

ultrasensitive real-time mass spectrometric analysis of vapors. Novartis Day, Zurich (Switzerland), Sep 2015

- Barrios-Collado, C.; Vidal-de-Miguel, G. *Modeling Space Charge effects in Transversal Modulation Ion Mobility Spectrometry*. 64th ASMS Conference on Mass Spectrometry and Allied Topics, San Antonio (Texas, USA), Jun 2016.

11.4.   Oral presentations as presenting author

- Barrios-Collado, C. *On the development of a Secondary Electrospray Ionization source for vapor analysis*. Seminar talk at ETH-Zürich. Jan 2015.
- Barrios-Collado, C. *Desarrollo de instrumentación apara análisis de vapores: LFSESI y TMIMS*. II Jornada de Doctorandos en el Programa de Doctorado en Ingeniería Industrial. Sep 2015.
- Barrios-Collado, C. *Avances en analizadores de vapores: aplicaciones prácticas y nuevos algoritmos de simulación.* III Jornada de Doctorandos en el Programa de Doctorado en Ingeniería Industrial. Sep 2016.

11.5.   Other publications

- Vidal-de-Miguel, G.; Macía, M.; Barrios, C.; Cuevas, J. *Transversal modulation ion mobility coupled with mass spectrometry: Exploring the IMS-IMS-MS possibilities of the instrument*. Analytical Chemistry, Volume 87, Issue 3, Pages 1925-1932, Jan 2015.
- García-Gómez, D.; Martínez-Lozano, P.; Barrios-Collado, C.; Vidal-de-Miguel, G.; Gaugg, M.; Zenobi, R. *Identification of 2-Alkenals, 4-Hydroxy-2-alkenals, and 4-Hydroxy-2,6-alkadienals in exhaled breath condensate by UHPLC-HRMS and in breath by real-time HRMS*. Analytical Chemistry, Volume 87, Issue 5, Pages 3087-3093, Feb 2015.
- García-Gómez, D.; Bregy, L.; Barrios-Collado, C.; Vidal-de-Miguel, G.; Zenobi, R. *Real-time high-resolution tandem mass spectrometry identifies furan derivatives in exhaled breath.* Analytical Chemistry, Volume 87. Issue 13, Pages 6919-6924, June 2015.
- García-Gómez, D.; Gaisl, T.; Barrios-Collado, C.; Vidal-de-Miguel, G.; Kohler, M.; Zenobi, R. *Real-time chemical analysis of e-cigarette aerosols by means of secondary electrospray ionization mass spectrometry.* Chemistry –A European Journal, Volume 22, Issue 7, Pages 2452-2457, Feb 2016.
- Gaugg, M.; García-Gómez, D.; Barrios-Collado, C.; Vidal-de-Miguel, G.; Kohler, M.; Zenobi, R.; Martinez-Lozano Sinues, P. *Expanding metabolite coverage of real-time breath analysis by coupling a universal secondary electrospray ionization source and high resolution mass spectrometry –a pilot study on tobacco smokers*. Journal of Breath Research, Volume 10, Issue 1, Pages 1-10, Feb 2016.

11.6. Other works presented at conferences

- Macia, M.; <u>Barrios, C.</u>; Vidal-de-Miguel, G. *Towards a functional ion mobility system for ion trap MS.* 62nd ASMS conference on Mass Spectrometry and Allied Topics, Baltimore, (Maryland, USA), Jun 2014
- García-Gómez, D.; Martínez-Lozano, P.; <u>Barrios-Collado, C.</u>; Vidal-de-Miguel, G.; Zenobi, R. *Identification of 2-alkenals, 4-hydroxy-2-alkenals and 4-hydroxy-2,6-alkadienals in exhaled breath condensate by UHPLC-HRMS and breath analysis in real time.* 42nd International Symposium on High Performance Liquid Phase Separations and Related Techniques; Geneva (Switzerland); Jun 2015
- García-Gómez, D.; Bregy, L.; <u>Barrios-Collado, C.</u>; Vidal-de-Miguel, G.; Zenobi, R. *Real-time high-resolution tandem mass spectrometry identifies furan derivatives in exhaled breath.* XX Reunión de la Sociedad Española de Química Analítica; Santiago de Compostela (Spain); Jul 2015
- Cuesta R., <u>Barrios-Collado C.</u>, Amo M., Fernandez de la Mora J., Tejero A., Martinez-Lozano Sinues P. *Low flow secondary electrospray ionization for volatile characterization delivers unique insights of biological and industrial processes*. VIII Reunión de la Sociedad Española de Espectrometría de Masas, Barcelona, Spain, (Jun 2017).

11.7. Press releases

- *Échame el aliento y te diré que dolencia padeces.* El Mundo. Jun 2015. http://www.elmundo.es/economia/2015/06/09/5575be94e2704eae218b4581.html
- *Numerical modeling and experimental validation of a universal secondary electrospray ionization source for mass spectrometric gas analysis in real-time.* Advances in Engineering. May 2016 https://advanceseng.com/chemical-engineering/numerical-modeling-experimental-validation-universal-secondary-electrospray-ionization-source-mass-spectrometric-gas-analysis-real-time/
- *Real Time Read-Out of Plant Metabolism*. Chimia. Sep 2016. http://www.ingentaconnect.com/contentone/scs/chimia/2016/00000070/00000009/art00010?crawler=true

12.   References

[1]   "Instrument Business Outlook," *Strategic Directions International, Inc*, vol. 19, p. 1, 2011.

[2]   B. . Eckenrode, "Environmental and forensic applications of field-portable GC-MS: an overview," *J. Am. Soc. Mass Spectrom.*, vol. 12, no. 6, pp. 683–693, 2001.

[3]   P. Martínez-Lozano, J. Rus, G. Fernández de la Mora, M. Hernández, and J. Fernández de la Mora, "Secondary Electrospray Ionization (SESI) of Ambient Vapors for Explosive Detection at Concentrations Below Parts Per Trillion," *J. Am. Soc. Mass Spectrom.*, vol. 20, no. 2, pp. 287–294, 2009.

[4]   M. J. Aernecke, T. Mendum, G. Geurtsen, A. Ostrinskaya, and R. R. Kunz, "Vapor Pressure of Hexamethylene Triperoxide Diamine (HMTD) Estimated Using Secondary Electrospray Ionization Mass Spectrometry," *J. Phys. Chem. A*, vol. 119, no. 47, pp. 11514–11522, Nov. 2015.

[5]   C. Wu, W. F. Siems, and H. H. Hill, "Secondary Electrospray Ionization Ion Mobility Spectrometry/Mass Spectrometry of Illicit Drugs," *Anal. Chem.*, vol. 72, no. 2, pp. 396–403, Jan. 2000.

[6]   L. Meier, C. Berchtold, S. Schmid, and R. Zenobi, "Sensitive detection of drug vapors using an ion funnel interface for secondary electrospray ionization mass spectrometry," *J. Mass Spectrom.*, vol. 47, no. 5, pp. 555–559, May 2012.

[7]   B. Ramoo, M. Funke, C. Frazee, and U. Garg, "Comprehensive Urine Drug Screen by Gas Chromatography/Mass Spectrometry (GC/MS).," *Methods Mol. Biol.*, vol. 1383, pp. 125–31, 2016.

[8]   J.-C. Wolf, M. Schaer, P. Siegenthaler, and R. Zenobi, "Direct Quantification of Chemical Warfare Agents and Related Compounds at Low ppt Levels: Comparing Active Capillary Dielectric Barrier Discharge Plasma Ionization and Secondary Electrospray Ionization Mass Spectrometry," *Anal. Chem.*, vol. 87, no. 1, pp. 723–729, Jan. 2015.

[9]   M. Kanamori-Kataoka and Y. Seto, "Measurement of breakthrough volumes of volatile chemical warfare agents on a poly(2,6-diphenylphenylene oxide)-based adsorbent and application to thermal desorption-gas chromatography/mass spectrometric analysis.," *J. Chromatogr. A*, vol. 1410, pp. 19–27, Sep. 2015.

[10] V. A. Krasnopolsky and V. A. Parshev, "Chemical composition of the atmosphere of Venus," *Nature*, vol. 292, no. 5824, pp. 610–613, Aug. 1981.

[11] P. Martínez-Lozano and J. F. de la Mora, "On-line Detection of Human Skin Vapors," *J. Am. Soc. Mass Spectrom.*, vol. 20, no. 6, pp. 1060–1063, 2009.

[12] J. Herbig, M. Müller, S. Schallhart, T. Titzmann, M. Graus, and A. Hansel, "On-line breath analysis with PTR-TOF," *J. Breath Res.*, vol. 3, no. 2, p. 27004, Jun. 2009.

[13] P. Martínez-Lozano and J. Fernández de la Mora, "Direct Analysis of Fatty Acid Vapors in Breath by Electrospray Ionization and Atmospheric Pressure Ionization-Mass Spectrometry," *Anal. Chem.*, vol. 80, no. 21, pp. 8210–8215, Nov. 2008.

[14] P. Martinez-Lozano, L. Zingaro, A. Finiguerra, and S. Cristoni, "Secondary electrospray ionization-mass spectrometry: breath study on a control group," *J Breath Res*, vol. 5, no. 1, p. 16002, Mar. 2011.

[15] P. Martínez-Lozano and J. F. de la Mora, "Electrospray ionization of volatiles in breath," 2007.

[16] P. Martínez-Lozano, "Mass spectrometric study of cutaneous volatiles by secondary electrospray ionization," *Int. J. Mass Spectrom.*, vol. 282, no. 3, pp. 128–132, 2009.

[17] N. G. Gotts, G. von Helden, and M. T. Bowers, "Carbon cluster anions: structure and growth from C5− to C62−," *Int. J. Mass Spectrom. Ion Process.*, vol. 149–150, pp. 217–229, Nov. 1995.

[18] B. C. Bohrer, S. I. Merenbloom, S. L. Koeniger, A. E. Hilderbrand, and D. E. Clemmer, "Biomolecule Analysis by Ion Mobility Spectrometry," *Annu. Rev. Anal. Chem.*, vol. 1, no. 1, pp. 293–327, Jul. 2008.

[19] M. F. Jarrold, "P EPTIDES AND P ROTEINS IN THE V APOR P HASE," *Annu. Rev. Phys. Chem.*, vol. 51, no. 1, pp. 179–207, Oct. 2000.

[20] S. L. Koeniger, S. I. Merenbloom, and D. E. Clemmer, "Evidence for Many Resolvable Structures within Conformation Types of Electrosprayed Ubiquitin Ions," *J. Phys. Chem. B*, vol. 110, no. 13, pp. 7017–7021, Apr. 2006.

[21] A. A. Shvartsburg, F. Li, K. Tang, and R. D. Smith, "Characterizing the structures and folding of free proteins using 2-D gas-phase separations: observation of multiple unfolded conformers.," *Anal. Chem.*, vol. 78, no. 10, pp. 3304–15, May 2006.

[22] M. M. Koek, R. H. Jellema, J. van der Greef, A. C. Tas, and T. Hankemeier, "Quantitative metabolomics based on gas chromatography mass spectrometry: status and perspectives.," *Metabolomics*, vol. 7, no. 3, pp. 307–328, Sep. 2011.

[23] J. H. Winnike, X. Wei, K. J. Knagge, S. D. Colman, S. G. Gregory, and X. Zhang, "Comparison of GC-MS and GC×GC-MS in the Analysis of Human Serum Samples for Biomarker Discovery," *J. Proteome Res.*, vol. 14, no. 4, pp. 1810–1817, Apr. 2015.

[24] K. Tekin, S. Karagöz, and S. Bektaş, "A review of hydrothermal biomass processing," *Renew. Sustain. Energy Rev.*, vol. 40, pp. 673–687, 2014.

[25] R. P. W. Scott, *Techniques and Practice of Chromatography*. CRC Press, 1995.

[26] J. Fernandez de la Mora, "Ionization of vapor molecules by an electrospray cloud," *Int. J. Mass Spectrom.*, vol. 300, no. 2–3, pp. 182–193, Mar. 2011.

[27] G. Vidal-de-Miguel and A. Herrero, "Secondary electrospray ionization of complex vapor mixtures. Theoretical and experimental approach.," *J. Am. Soc. Mass Spectrom.*, vol. 23, no. 6, pp. 1085–96, Jun. 2012.

[28] R. Mukhopadhyay, "IMS/MS: its time has come.," *Anal. Chem.*, vol. 80, no. 21, pp. 7918–20, Nov. 2008.

[29] G. A. Eiceman, Z. Karpas, H. H. Hill, and Jr., *Ion Mobility Spectrometry, Third Edition*. 2013.

[30] G. Vidal-de-Miguel, M. Macía, and J. Cuevas, "Transversal Modulation Ion Mobility Spectrometry (TM-IMS), a new mobility filter overcoming turbulence related limitations.," *Anal. Chem.*, vol. 84, no. 18, pp. 7831–7, Sep. 2012.

[31] M. Gamero-Castaño, "Beams of Electrosprayed Nanodroplets for Surface Engineering." University of California Irvine.

[32] P. Kiselev and J. B. Fenn, "ESIMS analysis of vapors at trace levels," in *Proceedings of the 49th ASMS Conference on Mass Spectrometry and Allied Topics May 27-31*, 2001.

[33] M. Tam and H. H. Hill, "Secondary Electrospray Ionization-Ion Mobility Spectrometry for Explosive Vapor Detection," *Anal. Chem.*, vol. 76, no. 10, pp. 2741–2747, May 2004.

[34] X. Li, P. Martinez-Lozano Sinues, R. Dallmann, L. Bregy, M. Hollmén, S. Proulx, S. A. Brown, M. Detmar, M. Kohler, and R. Zenobi, "Drug Pharmacokinetics Determined by Real-Time Analysis of Mouse Breath," *Angew. Chemie Int. Ed.*, vol. 54, no. 27, pp. 7815–7818, Jun. 2015.

[35] J. He, P. M.-L. Sinues, M. Hollmén, X. Li, M. Detmar, and R. Zenobi, "Fingerprinting Breast Cancer vs. Normal Mammary Cells by Mass Spectrometric Analysis of Volatiles," *Sci. Rep.*, vol. 4, pp. 225–249, Jun. 2014.

[36] P. Martínez-Lozano Sinues, R. M. Alonso-Salces, L. Zingaro, A. Finiguerra, M. V. Holland, C. Guillou, and S. Cristoni, "Mass spectrometry fingerprinting coupled to National Institute of Standards and Technology Mass Spectral search algorithm for pattern recognition," *Anal. Chim. Acta*, vol. 755, pp. 28–36, 2012.

[37] H. D. Bean, T. R. Mellors, J. Zhu, and J. E. Hill, "Profiling Aged Artisanal Cheddar Cheese Using Secondary Electrospray Ionization Mass Spectrometry," *J. Agric. Food Chem.*, vol. 63, no. 17, pp. 4386–4392, May 2015.

[38] C. Ballabio, S. Cristoni, G. Puccio, M. Kohler, M. R. Sala, P. Brambilla, and P. Martinez-Lozano Sinues, "Rapid identification of bacteria in blood cultures by mass-spectrometric analysis of volatiles," *J. Clin. Pathol.*, vol. 67, no. 8, pp. 743–746, Aug. 2014.

[39] J. Zhu, J. Jiménez-Díaz, H. D. Bean, N. A. Daphtary, M. I. Aliyeva, L. K. A. Lundblad, and J. E. Hill, "Robust detection of P. aeruginosa and S. aureus acute lung infections by secondary electrospray ionization-mass spectrometry (SESI-MS) breathprinting: from initial infection to clearance.," *J. Breath Res.*, vol. 7,

no. 3, p. 37106, Sep. 2013.

[40]   J. Zhu, H. D. Bean, J. Jiménez-Díaz, and J. E. Hill, "Secondary electrospray
       ionization-mass spectrometry (SESI-MS) breathprinting of multiple bacterial
       lung pathogens, a mouse model study.," *J. Appl. Physiol.*, vol. 114, no. 11, pp.
       1544–9, Jun. 2013.

[41]   G. Vidal-de-Miguel, M. Macía, P. Pinacho, and J. Blanco, "Low-Sample Flow
       Secondary Electrospray Ionization: Improving Vapor Ionization Efficiency,"
       Anal. Chem., vol. 84, no. 20, pp. 8475–8479, Oct. 2012.

[42]   G. Vidal-de-Miguel, "Add-on Secondary Electrospray Ionizer for pre-existing
       MS and for high sensitivity volatile analysis.," in *BIT's 4th Annual Conference
       EXPO of AnalytiX-2015*, 2015.

[43]   R. A. Sowell, S. L. Koeniger, S. J. Valentine, M. H. Moon, and D. E. Clemmer,
       "Nanoflow LC/IMS-MS and LC/IMS-CID/MS of protein mixtures.," *J. Am. Soc.
       Mass Spectrom.*, vol. 15, no. 9, pp. 1341–53, Sep. 2004.

[44]   S. L. Koeniger, S. I. Merenbloom, S. J. Valentine, M. F. Jarrold, H. R. Udseth, R.
       D. Smith, and D. E. Clemmer, "An IMS-IMS analogue of MS-MS.," *Anal.
       Chem.*, vol. 78, no. 12, pp. 4161–74, Jun. 2006.

[45]   K. Tang, A. A. Shvartsburg, H.-N. Lee, D. C. Prior, M. A. Buschbach, F. Li, A.
       V Tolmachev, G. A. Anderson, and R. D. Smith, "High-sensitivity ion mobility
       spectrometry/mass spectrometry using electrodynamic ion funnel interfaces.,"
       Anal. Chem., vol. 77, no. 10, pp. 3330–9, May 2005.

[46]   S. I. Merenbloom, R. S. Glaskin, Z. B. Henson, and D. E. Clemmer, "High-
       resolution ion cyclotron mobility spectrometry.," *Anal. Chem.*, vol. 81, no. 4, pp.
       1482–7, Feb. 2009.

[47]   S. I. Merenbloom, S. L. Koeniger, S. J. Valentine, M. D. Plasencia, and D. E.
       Clemmer, "IMS-IMS and IMS-IMS-IMS/MS for separating peptide and protein
       fragment ions.," *Anal. Chem.*, vol. 78, no. 8, pp. 2802–9, Apr. 2006.

[48]   M. S. Kelker, C. Berry, S. L. Evans, R. Pai, D. G. McCaskill, N. X. Wang, J. C.
       Russell, M. D. Baker, C. Yang, J. W. Pflugrath, M. Wade, T. J. Wess, and K. E.
       Narva, "Structural and biophysical characterization of Bacillus thuringiensis
       insecticidal proteins Cry34Ab1 and Cry35Ab1.," *PLoS One*, vol. 9, no. 11, p.
       e112555, Jan. 2014.

[49]   "Agilent | 6560 Ion Mobility Q-TOF LC/MS." [Online]. Available:
       http://www.agilent.com/en-us/products/mass-spectrometry/lc-ms-
       instruments/6560-ion-mobility-q-tof-lc-ms. [Accessed: 22-Nov-2015].

[50]   A. A. Shvartsburg and R. D. Smith, "Scaling of the resolving power and
       sensitivity for planar FAIMS and mobility-based discrimination in flow- and
       field-driven analyzers.," *J. Am. Soc. Mass Spectrom.*, vol. 18, no. 9, pp. 1672–81,
       Sep. 2007.

[51]   D. A. Barnett, M. Belford, J.-J. Dunyach, and R. W. Purves, "Characterization of

a temperature-controlled FAIMS system.," *J. Am. Soc. Mass Spectrom.*, vol. 18, no. 9, pp. 1653–63, Sep. 2007.

[52]   A. A. Shvartsburg, F. Li, K. Tang, and R. D. Smith, "High-resolution field asymmetric waveform ion mobility spectrometry using new planar geometry analyzers.," *Anal. Chem.*, vol. 78, no. 11, pp. 3706–14, Jun. 2006.

[53]   B. B. Schneider, T. R. Covey, S. L. Coy, E. V Krylov, and E. G. Nazarov, "Planar differential mobility spectrometer as a pre-filter for atmospheric pressure ionization mass spectrometry.," *Int. J. Mass Spectrom.*, vol. 298, no. 1–3, pp. 45–54, Dec. 2010.

[54]   B. B. Schneider, T. R. Covey, S. L. Coy, E. V Krylov, and E. G. Nazarov, "Chemical effects in the separation process of a differential mobility/mass spectrometer system.," *Anal. Chem.*, vol. 82, no. 5, pp. 1867–80, Mar. 2010.

[55]   B. B. Schneider, T. R. Covey, S. L. Coy, E. V Krylov, and E. G. Nazarov, "Control of chemical effects in the separation process of a differential mobility mass spectrometer system.," *Eur. J. Mass Spectrom. (Chichester, Eng).*, vol. 16, no. 1, pp. 57–71, Jan. 2010.

[56]   "SelexION Technology | SCIEX." [Online]. Available: http://sciex.com/products/ion-mobility-spectrometry/selexion-technology. [Accessed: 22-Nov-2015].

[57]   "Thermo FAIMS." [Online]. Available: http://www.thermoscientific.com/content/dam/tfs/ATG/CMD/cmd-support/ls-ms-systems/manuals/FAIMS-operators-manual.pdf. [Accessed: 22-Nov-2015].

[58]   K. Giles, S. D. Pringle, K. R. Worthington, D. Little, J. L. Wildgoose, and R. H. Bateman, "Applications of a travelling wave-based radio-frequency-only stacked ring ion guide.," *Rapid Commun. Mass Spectrom.*, vol. 18, no. 20, pp. 2401–14, Jan. 2004.

[59]   D. P. Smith, T. W. Knapman, I. Campuzano, R. W. Malham, J. T. Berryman, S. E. Radford, and A. E. Ashcroft, "Deciphering drift time measurements from travelling wave ion mobility spectrometry-mass spectrometry studies.," *Eur. J. Mass Spectrom. (Chichester, Eng).*, vol. 15, no. 2, pp. 113–30, Jan. 2009.

[60]   A. A. Shvartsburg and R. D. Smith, "Fundamentals of traveling wave ion mobility spectrometry.," *Anal. Chem.*, vol. 80, no. 24, pp. 9689–99, Dec. 2008.

[61]   "Ion Mobility Mass Spectrometry : Waters." [Online]. Available: http://www.waters.com/waters/en_GB/Ion-Mobility-Mass-Spectrometry/nav.htm?cid=134656158&locale=en_GB. [Accessed: 22-Nov-2015].

[62]   J. Fernández de la Mora, "The Differential Mobility Analyzer (DMA)," in *Ion Mobility Spectrometry - Mass Spectrometry*, 2010, pp. 105–136.

[63]   J. Rus, D. Moro, J. A. Sillero, J. Royuela, A. Casado, F. Estevez-Molinero, and J. Fernández de la Mora, "IMS–MS studies based on coupling a differential

mobility analyzer (DMA) to commercial API–MS systems," *Int. J. Mass Spectrom.*, vol. 298, no. 1–3, pp. 30–40, Dec. 2010.

[64]   P. Martínez-Lozano, E. Criado, G. Vidal, S. Cristoni, F. Franzoso, M. Piatti, and P. Brambilla, "Differential mobility analysis-mass spectrometry coupled to XCMS algorithm as a novel analytical platform for metabolic profiling," *Metabolomics*, vol. 9, no. S1, pp. 30–43, Jun. 2011.

[65]   C. J. Hogan and J. F. de la Mora, "Ion mobility measurements of nondenatured 12-150 kDa proteins and protein multimers by tandem differential mobility analysis-mass spectrometry (DMA-MS).," *J. Am. Soc. Mass Spectrom.*, vol. 22, no. 1, pp. 158–72, Jan. 2011.

[66]   "SEADM Mobility Front End." [Online]. Available: http://www.seadm.com/products/ion-mobility-add-ons-for-mass-specs/mobility-front-end-ion-mobility-filter/. [Accessed: 15-Jun-2016].

[67]   J. L. Neves, P. E. Haigh, C. Wu, and W. J. McGann, "ITMS-MS analysis of smokeless powder," *Int. J. Ion Mobility Spectrom*, 2003. .

[68]   F. A. Fernandez-Lima, D. A. Kaplan, and M. A. Park, "Note: Integration of trapped ion mobility spectrometry with mass spectrometry.," *Rev. Sci. Instrum.*, vol. 82, no. 12, p. 126106, Dec. 2011.

[69]   "ChemPro100i - Environics Oy." [Online]. Available: http://www.environics.fi/product/chempro100i/. [Accessed: 22-Nov-2015].

[70]   "ChemRAE." [Online]. Available: http://www.raesystems.com/sites/default/files/content/resource/FeedsEnclosure-ChemRAE_US_DS.pdf. [Accessed: 22-Nov-2015].

[71]   R. T. Kurulugama, F. M. Nachtigall, S. Lee, S. J. Valentine, and D. E. Clemmer, "Overtone mobility spectrometry: part 1. Experimental observations.," *J. Am. Soc. Mass Spectrom.*, vol. 20, no. 5, pp. 729–37, May 2009.

[72]   S. J. Valentine, S. T. Stokes, R. T. Kurulugama, F. M. Nachtigall, and D. E. Clemmer, "Overtone mobility spectrometry: part 2. Theoretical considerations of resolving power.," *J. Am. Soc. Mass Spectrom.*, vol. 20, no. 5, pp. 738–50, May 2009.

[73]   S. J. Valentine, R. T. Kurulugama, and D. E. Clemmer, "Overtone mobility spectrometry: part 3. On the origin of peaks.," *J. Am. Soc. Mass Spectrom.*, vol. 22, no. 5, pp. 804–16, May 2011.

[74]   R. T. Kurulugama, F. M. Nachtigall, S. J. Valentine, and D. E. Clemmer, "Overtone mobility spectrometry: part 4. OMS-OMS analyses of complex mixtures.," *J. Am. Soc. Mass Spectrom.*, vol. 22, no. 11, pp. 2049–60, Nov. 2011.

[75]   M. A. Ewing, S. M. Zucker, S. J. Valentine, and D. E. Clemmer, "Overtone mobility spectrometry: part 5. Simulations and analytical expressions describing overtone limits.," *J. Am. Soc. Mass Spectrom.*, vol. 24, no. 4, pp. 615–21, Apr. 2013.

[76]   G. Vidal-de-Miguel, "Method and apparatus to produce steady beams of mobility selected ions via time-dependent electric fields," 8,378,297 B2.

[77]   G. Vidal-de-Miguel, M. Macía, C. Barrios, and J. Cuevas, "Transversal Modulation Ion Mobility Spectrometry (IMS) Coupled with Mass Spectrometry (MS): Exploring the IMS-IMS-MS Possibilities of the Instrument," *Anal. Chem.*, vol. 87, no. 3, pp. 1925–1932, 2015.

[78]   V. K. Rawat, G. Vidal-de-Miguel, and C. J. Hogan, "Modeling vapor uptake induced mobility shifts in peptide ions observed with transversal modulation ion mobility spectrometry-mass spectrometry.," *Analyst*, vol. 140, no. 20, pp. 6945–54, Sep. 2015.

[79]   N. A. Meyer, K. Root, R. Zenobi, and G. Vidal-de-Miguel, "Gas-Phase Dopant-Induced Conformational Changes Monitored with Transversal Modulation Ion Mobility Spectrometry.," *Anal. Chem.*, vol. 88, no. 4, pp. 2033–40, Feb. 2016.

[80]   "FIT TMIMS." [Online]. Available: http://www.fossiliontech.com/tmims/. [Accessed: 15-Jun-2016].

[81]   G. Vidal-de-Miguel, M. Macía, J. Cuevas, and C. Barrios, "Transversal Modulation IMS. (TM-IMS) 'Path to next-generation IMS: new concepts, advanced instrumentation, and leveraging the ion-molecule chemistry,'" in *19th International Mass Spectrometry Conference*, 2012.

[82]   G. Vidal-de-Miguel, "Transversal Modulation Ion Mobility Spectrometer with reduced voltage and improved robustness and resolving power," USPTO 62/114,601.

[83]   G. Vidal-de-Miguel, "Method and apparatus to generate beams of ions with controlled ranges of mobilities," 62/077,412.

[84]   J. F. De La Mora, "The effect of charge emission from electrified liquid cones," *J. Fluid Mech.*, vol. 243, no. 1, p. 561, Oct. 1992.

[85]   N. A. Fuchs and A. G. Sutugin, *Highly Dispersed Aerosols*. John Wiley & Sons, Inc, 1969.

[86]   P. Martinez-Lozano Sinues, E. Criado, and G. Vidal, "Mechanistic study on the ionization of trace gases by an electrospray plume," *Int. J. Mass Spectrom.*, vol. 313, pp. 21–29, 2012.

[87]   J. Zhao and R. Zhang, "Proton transfer reaction rate constants between hydronium ion (H3O+) and volatile organic compounds," *Atmos. Environ.*, vol. 38, no. 14, pp. 2177–2185, 2004.

[88]   C. Barrios-Collado and G. Vidal-de-Miguel, "Numerical algorithm for the accurate evaluation of ion beams in transversal modulation ion mobility spectrometry: Understanding realistic geometries," *Int. J. Mass Spectrom.*, vol. 376, pp. 97–105, 2015.

[89]   F. Loreto and J.-P. Schnitzler, "Abiotic stresses and induced BVOCs.," *Trends*

Plant Sci., vol. 15, no. 3, pp. 154–66, Mar. 2010.

[90] U. Hansen and G. Seufert, "Temperature and light dependence of β-caryophyllene emission rates," *J. Geophys. Res. Atmos.*, vol. 108, no. D24, p. n/a-n/a, Dec. 2003.

[91] M. D'Alessandro, M. Held, Y. Triponez, and T. C. J. Turlings, "The Role of Indole and Other Shikimic Acid Derived Maize Volatiles in the Attraction of Two Parasitic Wasps," *J. Chem. Ecol.*, vol. 32, no. 12, pp. 2733–2748, Dec. 2006.

[92] V. V. Roshchina and V. D. Roshchina, *The Excretory Function of Higher Plants.* Berlin, Heidelberg: Springer Berlin Heidelberg, 1993.

[93] E. W. Chehab, R. Kaspi, T. Savchenko, H. Rowe, F. Negre-Zakharov, D. Kliebenstein, and K. Dehesh, "Distinct roles of jasmonates and aldehydes in plant-defense responses," *PLoS One*, vol. 3, no. 4, 2008.